RSC Advances

PAPER

View Article Online
View Journal | View Issue

Cite this: *RSC Adv.*, 2026, **16**, 17021

Interfacial charge transfer-driven UV-activated photocatalytic degradation of metronidazole *via* δ-MnO_2/WO_3 heterojunction in aqueous media

Md Shafayatul Islam,[a] Mehedi Hasan Prince,[b] Koushik Roy Chowdhury,[a] Sifat Sharmin Rawfa,[c] Ilma Jahan Ritu,[d] S. M. Khalid Hossain[a] and Ahmed Sharif *[a]

Pharmaceutical contaminants, particularly recalcitrant antibiotics such as metronidazole (MNZ), are removed from water by engineering an efficient UV-driven δ-MnO_2/WO_3 nano-heterojunction photocatalyst to reduce public health risk and restore ecosystems. In this study, a novel hierarchical nanocomposite photocatalyst was synthesized *via* a facile two-step hydrothermal route with unique "flower-rod" architectures. Structural and surface analyses confirm the presence of pure δ-MnO_2 and hexagonal WO_3, as well as reveal the coherent interfaces between the flower-shaped δ-MnO_2 and rod-shaped hexagonal WO_3. The nanocomposite exhibited reduced crystallite size, higher micro-strain, and defect-rich surfaces compared to pure phases, which are favorable for charge trapping and adsorption. UV-Vis diffuse reflectance spectroscopy detected broad UV-visible absorption and a slight band gap widening upon coupling, while band-edge calculations indicated a type-I alignment between δ-MnO_2 and WO_3. The photocatalytic performance assessed by the MNZ degradation under UV light irradiation demonstrated that the δ-MnO_2/WO_3 (5%) photocatalyst achieved ~82% degradation within 100 min at an optimal dosage of 0.5 g L^{-1} and pH 11, outperforming pristine δ-MnO_2 and WO_3. The corresponding pseudo-first-order rate constant (0.01541 min^{-1}) and electrochemical impedance spectroscopy revealed evidence of fast kinetics, lower charge-transfer resistance, and more efficient separation of photogenerated carriers. These results emphasize δ-MnO_2/WO_3 nano-heterojunctions as a promising and highly efficient photocatalytic treatment for antibiotic-contaminated wastewater.

Received 1st February 2026
Accepted 20th March 2026

DOI: 10.1039/d6ra00866f

rsc.li/rsc-advances

1. Introduction

The rapid pace of urbanization has led to significant environmental issues, including air, water, and other resource pollution and soil degradation.[1,2] Industrial activities contribute significantly to water pollution by generating effluents containing complex organic chemicals, such as antibiotics, fertilizers, insecticides, plasticizers, and organic colorants.[1,3] These substances are byproducts of various manufacturing processes and are often used directly in healthcare facilities, ultimately being released into rivers and sewage systems. Among these chemicals, antibiotics are particularly challenging to remove from the environment due to their high chemical stability. Antibiotics are commonly classified into six major pharmacological groups: aminoglycosides, glycopeptides, macrolides, β-lactams, quinolones, and tetracyclines.[4] Apart from these six major antibiotic classes, another important group in the context of environmental and health concerns is the nitroimidazoles, which include metronidazole (MNZ). MNZ is commonly used to treat bacterial infections, a range of protozoan diseases, and *Giardia* infections in various animals, including dogs and cats.[5,6] According to previous studies, MNZ is highly soluble in water and not biodegradable; unintentional exposure to it may reduce our resistance to harmful microorganisms.[6,7] In an aquatic environment, the presence of MNZ may disrupt the final step of the nitrogen cycle carried out by anaerobic bacteria, in which nitrate is converted to nitrous gas. This disruption may lead to nitrate buildup, increasing the risk of infections, tissue damage, and physiological stress in aquatic species.[8] It may also hamper the blood oxygen transfer and cause renal failure.[9] Therefore, developing an efficient, cost-effective method for MNZ removal is critical.

Previously, various conventional processes, such as adsorption, ion exchange, sedimentation, reverse osmosis, and electrocoagulation, were used to remove pollutants from wastewater.[3,10–12] However, most of these processes have multiple drawbacks, such as low efficiency, high cost, and the formation of secondary pollutant agents. To address these

[a]*Department of Materials and Metallurgical Engineering, Bangladesh University of Engineering and Technology, Dhaka 1000, Bangladesh. E-mail: asharif@mme.buet.ac.bd*

[b]*Department of Materials Science & Engineering, Rensselaer Polytechnic Institute (RPI), NY, 12180, USA*

[c]*Department of Mathematics, University of Dhaka, Dhaka – 1000, Bangladesh*

[d]*Magura Medical College, Magura, 7600, Bangladesh*

issues, advanced oxidation processes (AOPs), such as photocatalytic oxidation, the photo-Fenton, electro-Fenton, and ozonation, have been developed and are effectively employed to degrade harmful organic pollutants in wastewater.[10] Although the Fenton process is regarded as one of the most effective methods for degrading various organic substances at atmospheric temperatures, it has several limitations, including the need for acidic pH and difficulties in catalyst recovery.[7] These limitations may be addressed by the photocatalytic oxidation process,[13] which can operate over a broader pH range, facilitate easier catalyst recovery, have low operating costs, operate at atmospheric temperatures and pressures, and pose minimal risk of secondary contamination.[1,12]

Various transition-metal oxides, including MnO_2, V_2O_5, CuO, and WO_3, are extensively studied for their potential in energy storage and photocatalytic applications because of their high stability and abundance.[14–16] Among these, δ-MnO_2 is particularly interesting because of its layered birnessite-type structure, which provides a high-density redox active site and large interlayer spacing, which can facilitate ion and molecular diffusion.[17] MnO_2-based nanostructures have already been reported to show promising photocatalytic activity. For example, Das *et al.* demonstrated that flower-shaped δ-MnO_2 degrades organic dyes very efficiently *via* photocatalysis under sunlight.[18] Moreover, δ-MnO_2 exhibited superior photocatalytic activity compared to α-MnO_2, attributed to its favorable band structure and increased number of active sites (97% MB degradation in 60 min sunlight *vs.* 83% in 120 min UV). Similarly, Alinda Shaly *et al.* reported that hydrothermally synthesized α-MnO_2 nanowires have a lower bandgap of approximately 0.99 eV, achieving ∼51.5% tetracycline degradation within 70 minutes, thereby highlighting their potential for antibiotic removal and environmental remediation.[19] However, pristine MnO_2 has some drawbacks, such as low electrical conductivity and a high rate of electron–hole recombination, which significantly hinder its photocatalytic efficiency.[20]

Another transition metal oxide, WO_3, is noteworthy for its relatively narrow band gap of approximately 2.6–2.8 eV. This allows it to absorb UV and visible light, which makes it well-suited for photocatalytic applications across a wide range of irradiation conditions. Szilágyi *et al.* showed that the photocatalytic performance of WO_3 strongly depends on its oxidation state, with fully oxidized monoclinic WO_3 exhibiting the highest activity for both aqueous and gas-phase pollutant degradation.[21] Similarly, Sánchez Martínez *et al.* reported that WO_3 nanoparticles synthesized *via* a urea-assisted precipitation method and calcined at 500 °C showed the highest photocatalytic activity. These nanoparticles effectively degraded organic dyes, including indigo carmine, rhodamine B, and Congo red, upon exposure to visible light, with indigo carmine achieving the highest level of mineralization.[22] In recent years, semiconductor heterojunctions have emerged as an effective means to overcome the intrinsic limitations of single-component photocatalysts. By integrating two semiconductors with appropriately aligned bands, these heterojunctions may facilitate the effective separation of photogenerated electron–hole pairs, minimize recombination losses, and broaden the light-absorption spectrum. Several charge-transfer mechanisms, such as type-I, type-II, Z-scheme, and S-scheme heterojunctions, have been suggested to account for the improved photocatalytic activity. Among them, metal oxide-metal oxide heterojunctions stand out due to their chemical stability, straightforward synthesis, and suitability for large-scale water treatment.

While MnO_2-based composites and WO_3-based heterojunction photocatalysts have been widely explored in the literature, the present work advances the field in several specific and meaningful ways that go beyond prior reports. First, earlier studies on MnO_2-based photocatalysts typically involve coupling MnO_2 with g-C_3N_4, carbon materials, or other semiconductors to enhance charge separation and pollutant degradation efficiency.[23] However, those systems do not specifically control the crystal phase of MnO_2 or investigate its interaction with WO_3 in a well-defined δ-MnO_2/WO_3 heterojunction. Second, WO_3 is recognized as a visible-light-active semiconductor with high stability and high hole mobility, and various strategies, such as oxygen-vacancy engineering and heterojunction construction, have been explored to improve its photocatalytic performance.[24] Nonetheless, most reported WO_3-based studies focus on forming heterojunctions with materials such as g-C_3N_4, TiO_2, or other oxides rather than on specifically engineering the δ-MnO_2/WO_3 interface to optimize band alignment. The novelty of the present work lies in the targeted construction of a δ-MnO_2/WO_3 heterojunction, in which the layered δ-MnO_2 phase and tunnel-structured WO_3 combine to create a unique interface that enhances interfacial charge transfer and suppresses electron–hole recombination more effectively than in random composites. Additionally, unlike many reports that rely on simple physical mixing, our synthesis approach yields intimate interfacial contact with phase-controlled morphology, thereby improving light absorption and catalytic activity under visible light.

To the best of the author's knowledge, a comprehensive study of the photocatalytic property of δ-MnO_2/WO_3 has not been explored. Therefore, in this work, δ-MnO_2/WO_3 composite was used to degrade Metronidazole in water. The flower-rod morphology of δ-MnO_2/WO_3, as reported in our previous work[25] promotes efficient charge separation, enhanced electron-transport pathways, and abundant defect-rich surfaces. These features can enhance the production of reactive species like $OH^{\bullet}$ and $^{\bullet}O_2^-$ radicals, which are essential for breaking down antibiotics. Additionally, adding WO_3 nanorods is likely to improve structural stability and introduce more redox-active centers, addressing the conductivity and stability issues associated with MnO_2.

2. Experimental

2.1. Materials

Analytical grade potassium permanganate ($KMnO_4$, ≥99%), manganese(II) sulfate monohydrate ($MnSO_4 \cdot H_2O$, ≥99%), sodium chloride (NaCl, ≥99.5%), hydrochloric acid (HCl, 37%), sodium tungstate dihydrate ($Na_2WO_4 \cdot 2H_2O$, ≥99%), and citric acid monohydrate (≥99.5%) were used as precursors. The

highest purity deionized (DI) water, with a resistivity of 18.2 MΩ cm, was used to prepare all aqueous solutions. Merck (Germany) supplied all chemicals.

2.2. Preparation of pure δ-MnO_2, pure WO_3, δ-MnO_2/WO_3 composite

The δ-MnO_2/WO_3 composite was produced using a two-step hydrothermal process. Initially, 33.5 mmol $KMnO_4$ and 9.5 mmol $MnSO_4 \cdot H_2O$ were dissolved in 160 mL of deionized water to create a uniform solution. The mixture was gently stirred for an hour until it turned into a smooth, uniform pink solution. After that, it was transferred to a Teflon-lined stainless-steel autoclave. The autoclave was carefully heated to 140 °C for approximately 30 minutes; then it was cooled down to room temperature. The black powder was rinsed three times with ethanol and three times with water through centrifugation, discarding the liquid after each rinse. Ultimately, flower-shaped δ-MnO_2 was produced by vacuum-drying the powder overnight at 70 °C.

Then, $Na_2WO_4 \cdot 2H_2O$ was dissolved in 160 mL of distilled water and stirred with a magnetic stirrer until the solution was homogeneous. A 3 M HCl aqueous solution was then added dropwise to bring the pH to about 2. After stirring for two hours, the resulting greenish-yellow solution was transferred into a 250 mL autoclave and heated at 200 °C for 20 hours. Upon cooling to room temperature, the precipitates were collected, washed, and dried to yield h-WO_3 nanorods.

Finally, 5 wt% amount of WO_3 nanorods was dispersed in 60 mL of distilled water and sonicated for 1 h using a probe sonicator. In a separate step, a 110 mL solution containing $MnSO_4 \cdot H_2O$ and excess $KMnO_4$ was sonicated, then combined with the WO_3 suspension. The mixture was stirred vigorously for 1–2 hours. It was then transferred to a Teflon-lined autoclave and heated to 140 °C for 30 minutes. After cooling, the product was washed and dried at 70 °C for 12–14 hours to produce the δ-MnO_2/WO_3 composite. The whole process of making the δ-MnO_2, WO_3, and δ-MnO_2/WO_3 composite is shown in Fig. 1.

2.3. Characterization

An X-ray diffractometer (Rigaku) with Cu $K_{\alpha1}$ (1.5406 Å) and $K_{\alpha2}$ (1.5444 Å) radiation was used to perform room-temperature structure and phase analysis of the samples. The scan rate was 5° per minute, and the diffraction pattern was recorded over a 2θ range of 10–80. To analyze the surface morphology and microstructure of the samples, a Field Emission Scanning Electron Microscope (FESEM: JEOL JSM 7600F) and a transmission electron microscope (TEM: Talos F200X, Thermo Fisher Scientific, USA) were employed. Micrographs taken from SEM and TEM were processed and analyzed with Gatan software and ImageJ. Additionally, the surface chemical and oxidation

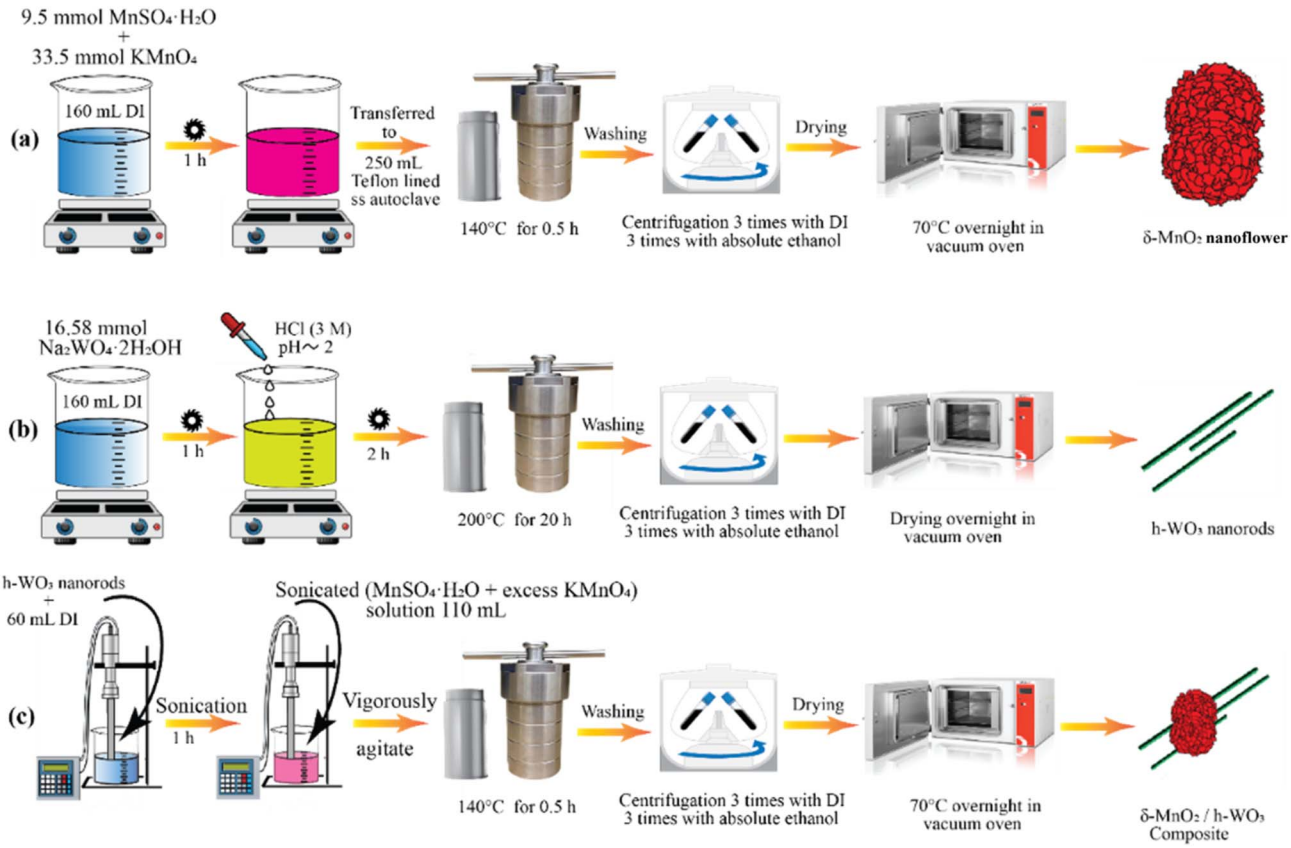

Fig. 1 Schematic diagram showing the step-by-step synthesis routes for δ-MnO_2 (a), WO_3 (b), and δ-MnO_2/WO_3 (c) composite photocatalysts used in this study.

states of the elements were investigated using X-ray photoelectron spectroscopy (XPS) on a Thermo Fisher Scientific Escalab Xi+ instrument equipped with a monochromatic Al Kα source.

2.4. Photocatalytic degradation process

The sample's photocatalytic activity was evaluated by degrading 100 mL of an aqueous Metronidazole (MNZ) solution at an initial concentration of 10 ppm. Different amounts of photocatalyst (0.4, 0.5, and 0.6 g L^{-1}) were then added to the solution. The mixture of the photocatalyst and MNZ was stirred in the dark for 30 minutes to reach adsorption–desorption equilibrium before exposing it to light. Afterward, the suspension was exposed to UV light with constant stirring to ensure even catalyst distribution and consistent light exposure. At designated time intervals, 10 mL samples of the solution were taken, centrifuged to eliminate photocatalyst particles, and the residual MNZ concentration was determined using UV-vis spectroscopy. The absorption peak appeared at 319 nm, and the degradation efficiency was assessed using the normalized concentration ratio (C/C_0), where C_0 denotes the initial MNZ concentration after dark adsorption equilibrium, and C is the concentration at time t during irradiation.

The recyclability of the δ-MnO_2/WO_3 (5%) photocatalyst was tested over five consecutive degradation cycles under identical conditions. After each 80-minute irradiation, the catalyst was separated *via* centrifugation, thoroughly washed with deionized water and ethanol to remove residual intermediates, and dried at 60 °C before reuse. The recovered catalyst was then added to a fresh metronidazole solution at the same initial concentration and with the same amount of photocatalyst for the next cycle. To determine the main reactive species radical scavenger tests were carried out. Isopropanol (IPA), *p*-benzoquinone (BQ) and EDTA were used as scavengers for $^{\bullet}OH$, $^{\bullet}O_2^-$, and h^+ respectively. For the experiment, 1 mM scavenger and 0.5 g per L δ-MnO_2/WO_3 (5%) were added to 100 mL 10 ppm metronidazole solution.

3. Results and discussion

3.1. Structural analysis

The powder diffraction patterns at room temperature for the synthesized samples (δ-MnO_2, WO_3, and the δ-MnO_2/WO_3 (5%) nanocomposite) are presented in Fig. 2. The XRD pattern of δ-MnO_2 exhibits characteristic reflections indexed to the (001), (002), and (020) planes, consistent with JCPDS PDF No. 80–1098.[26] The space group of the material is $C2/m$, with unit cell parameters of $a = 5.149$ Å, $b = 2.843$ Å, $c = 7.176$ Å, and $\beta = 100.76°$. The XRD analysis verifies that the pristine δ-MnO_2 has a base-centered monoclinic lattice structure, and the lack of additional XRD lines indicates its purity. Fig. 2(b) shows that the diffraction peaks of WO_3 match well with those of hexagonal WO_3 (JCPDS No. 33-1387). The presence of sharp, strong diffraction peaks confirms high crystallinity. The absence of extra peaks indicates phase purity.[27,28] Fig. 2(c) represents the XRD pattern of the prepared δ-MnO_2/WO_3 nanocomposite. All significant peaks of δ-MnO_2 and WO_3 are observable in the δ-MnO_2/WO_3 (5%) spectra, indicating the incorporation of WO_3 into δ-MnO_2 and formation of a nanocomposite without any heterogeneous phase and structural damage. Overlapping diffraction peak at the angle $2\theta = 36.60°$ corresponds to the $(\bar{1}11)$ plane of δ-MnO_2 and (201) plane of WO_3, leading to fluctuations in peak intensity and a slight increase in the peak's intensity at 36.60° in the heterostructure XRD pattern, confirming the successful synthesis of δ-MnO_2/WO_3.[29,30] Some low-intensity reflections of WO_3 can't be observed in the composite pattern because of its small fraction in the composite. No additional diffraction peaks from contaminants were observed, indicating the purity of the δ-MnO_2/WO_3 binary catalyst. The

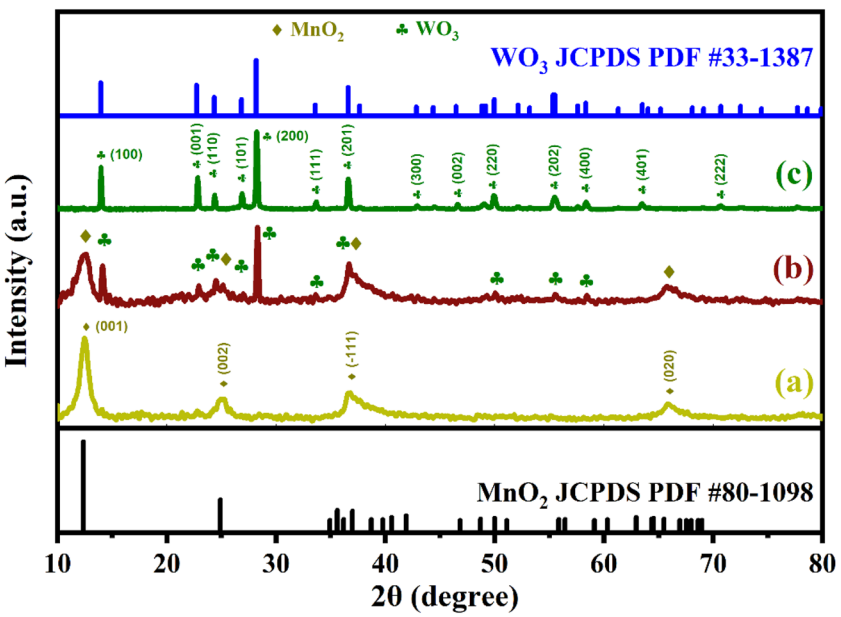

Fig. 2 X-ray diffraction patterns of (a) pristine δ-MnO_2, (b) δ-MnO_2/WO_3 (5%) composite, and (c) hexagonal WO_3.

Table 1 Crystallite size, degree of crystallinity, micro-strain, and dislocation density of δ-MnO_2, WO_3, and δ-MnO_2/WO_3 (5%)

Nanoparticles	Crystallite size, D_c (nm)	Degree of crystallinity (%)	Micro-strain (ε)	Dislocation density, δ (10^{15} lines per m^2)
δ-MnO_2	7.38	38.49	0.043	18.36
WO_3	37.20	55.85	0.004	0.723
δ-MnO_2/WO_3 (5%)	5.77	44.07	0.056	29.99

Scherrer equation (eqn (1)) was used to calculate the crystallite sizes (D_c) of prepared samples, and the degree of crystallinity was determined by using eqn (2).[31,32]

$$D_c = \frac{K_B \lambda}{\beta \cos \theta} \quad (1)$$

$$\text{Degree of crystallinity} = \frac{A_{CP}}{A_{CP} + A_{AP}} \times 100\% \quad (2)$$

where, K_B denotes Scherrer's broadening constant, which varies between 0.8 and 1.1 based on crystal morphology, with a typical value of 0.9,[33] λ indicates the wavelength of the Cu Kα radiation used, which is 0.15406 nm. β indicates the full width at half maximum (FWHM) of the diffraction peak in degrees, and θ represents the Bragg diffraction angle. A_{CP} is the area under the crystalline peaks, and A_{AP} corresponds to the diffuse background (non-crystalline) contribution. Eqn (3) and (4) were used to calculate the micro strain (ε) and dislocation density (δ) of the samples. All the values of crystallite size, degree of crystallinity, micro-strain, and dislocation density for δ-MnO_2, WO_3, and δ-MnO_2/WO_3 (5%) are represented in Table 1.

$$\varepsilon = \frac{\beta}{4 \tan \theta} \quad (3)$$

$$\delta = \frac{1}{(D_c)^2} \quad (4)$$

Crystallographic parameters of δ-MnO_2 and the δ-MnO_2/WO_3 (5%) composite have been calculated using the (001) crystal plane, and for WO_3, the (200) plane has been used.

The smaller crystallite size in the nanocomposite suggests a higher surface area, potentially enhancing photocatalyst adsorption. An increase in micro-strain and dislocation density may create defects that trap charges and impede the recombination of electron–hole pairs. This process may enhance charge separation and boost the photocatalytic activity of the nanocomposite.[34,35]

3.2. Morphological analysis

Scanning electron microscopy (SEM) images of as-prepared δ-MnO_2, WO_3, and δ-MnO_2/WO_3 (5%) nanocomposites were examined at different magnifications to investigate the surface morphology. Fig. 3(a and b) shows the bare δ-MnO_2 nanoflower with an array of folded nanosheets with a petal-like flake morphology. These numerous nanopetals, with varying thicknesses, extend outward from the crystal's center and represent the marigold nanoflower morphology.[36] The three-dimensional structure indicated that the average nanoflower diameter is 491 nm. Fig. 3(c and d) demonstrates that pure WO_3 displays a nanorod morphology, with the average nanorod length of 1.3 μm. WO_3 nanorod in nanocomposite is smaller than bare WO_3 particles because of the intertwined growth of hexagonal WO_3 on δ-MnO_2 surface, which suggests that δ-MnO_2 may significantly reduce the growth of WO_3 nanorods.[37,38] The hexagonal tunnel structure of WO_3 nanorods may facilitate interfacial charge transfer between δ-MnO_2 nanoflowers, thereby improving photocatalytic performance.[39] Fig. 3(e and f) demonstrates that nanorods are consistently interconnected, resulting in the formation of hierarchical bundles, which confirms that the δ-MnO_2/WO_3 (5%) nanocomposite has WO_3 nanorods supported on flower-like δ-MnO_2 sheets in close contact and forms a binary δ-MnO_2/WO_3 nanocomposite.[40] This integration increases surface area and establishes close contact between the two components, which is essential for antibiotic degradation.[41]

Transmission electron microscopy (TEM) and high-resolution TEM (HRTEM) were used to obtain more detailed microstructural information about the synthesized nanoparticles, as shown in Fig. 4(a–i). The TEM images in Fig. 4(e and f) show densely packed nanoparticles with distinct interfaces between δ-MnO_2 and WO_3. The selected-area electron diffraction (SAED) pattern of MnO_2 provided in the S1 indicates a diffraction ring of corresponding $(\bar{1}11)$ and (020) plane, confirming the weak crystallinity of δ-MnO_2 nanoflowers, consistent with earlier findings from XRD analysis. The concentric circles in the SAED pattern indicate the crystalline structure of the agglomerated WO_3 particles, and the pattern shows spots aligned with the hexagonal WO_3 zone axis, confirming the whole structure.[42,43] HRTEM analysis shows that a lattice spacing of 0.367 nm matches the (110) plane of hexagonal WO_3, as shown in Fig. 4(i). Additionally, the lattice spacing of 0.720 nm, related to the (001) plane of δ-MnO_2 in the composite, is noticeably larger than the 0.703 nm of the (001) plane of pure MnO_2. This increase in interplanar distance in the composite likely results from W^{6+} ion integration into the MnO_2 interlayer.[34]

3.3. XPS analysis

The surface composition and chemical states of different elements in δ-MnO_2 and δ-MnO_2/WO_3 nanocomposites were examined utilizing X-ray Photoelectron Spectroscopy (XPS). The survey spectra for pure δ-MnO_2 and the δ-MnO_2/WO_3 (5%) composite, within the binding energy range of 0 to 1200 eV, are depicted in Fig. 5. The spectra for δ-MnO_2 confirm the presence

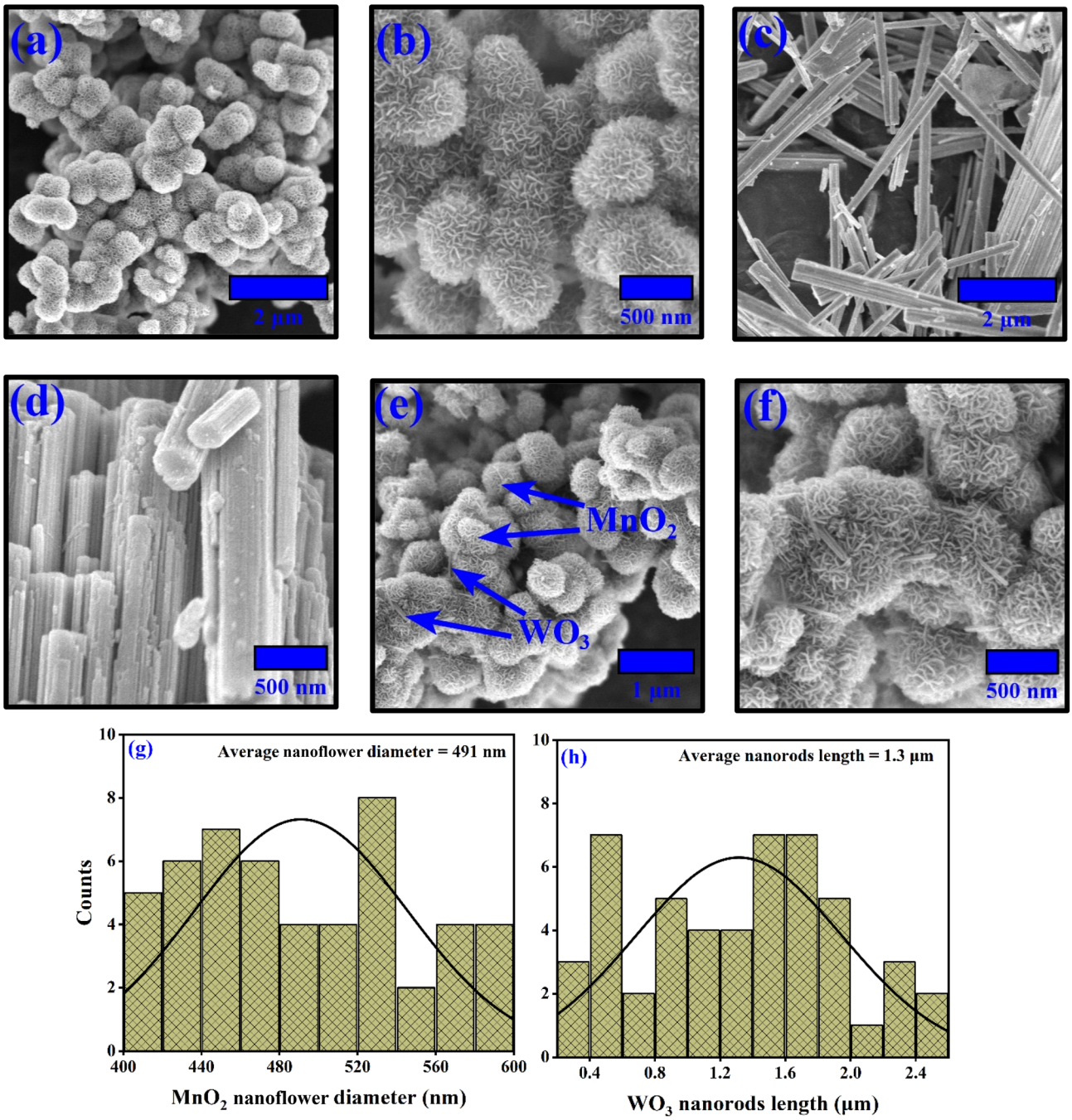

Fig. 3 FESEM images illustrating the surface morphology of the synthesized samples (a and b), with pure MnO_2 displaying a hierarchical nanoflower-like structure architectures; (c and d) pure WO_3 displaying nanorod-like structures with relatively uniform alignment; (e and f) δ-MnO_2/WO_3 (5%) composite, where WO_3 nanorods are uniformly distributed on the MnO_2 nanoflower surface; (g) statistical size distribution of MnO_2 nanoflowers indicates an average diameter of about 491 nm. Additionally, (h) the length distribution histogram of WO_3 nanorods shows an average length of approximately 1.3 μm.

of Mn and O, while the δ-MnO_2/WO_3 (5%) composite also shows W alongside Mn and O. Carbon was detected in all samples, as evidenced in the high-resolution spectra (Fig. 6 and 7), likely due to unavoidable surface contamination from air exposure and handling.

High-resolution spectra for C 1s, Mn 2p, and O 1s from pure δ-MnO_2 are presented in Fig. 6. The O 1s spectrum deconvolution reveals three distinct peaks: a low-binding-energy peak at 529.78 eV corresponding to manganese–oxygen in the atomic lattice, an intermediate peak at 531.28 eV attributed to oxygen vacancies, and a high-binding-energy peak at 532.95 eV associated with water molecules (O–H) adsorbed on the surface.[44–46] Adsorbed gaseous oxygen on the surface can generate oxygen vacancies in MnO_2, leading to the formation of

surface oxygen species such as Mn–OH. As a result, the concentration of surface oxygen species is directly linked to surface oxygen vacancies, thereby enhancing the photocatalyst's photocatalytic activity.[47–50]

The majority of oxygen is associated with manganese as Mn–O–Mn and Mn–OH, which indicates the potential for additional active sites and promotes the degradation reaction.[41,51] The high-resolution fitted spectrum of the Mn 2p doublet confirms the Mn^{4+} oxidation state, showing an 11.6 eV spin energy separation between the Mn $2p_{1/2}$ (653.3 eV) and Mn $2p_{3/2}$ (641.7 eV) states.[36,52–54]

Fig. 7 presents the high-resolution spectra from the composite, showing the existence of C, Mn, and O. Additionally, peaks corresponding to W 4f were observed, originating from WO_3. The deconvoluted W 4f spectrum reveals four distinct peaks, which correspond to the W $4f_{5/2}$ and W $4f_{7/2}$ levels.[53,55,56] The peaks observed at binding energies of 35.3 and 37.6 eV correspond to the W^{6+} state. In contrast, peaks at 34.1 and 36.9 eV correspond to the W^{5+} state, which may result from the photoemission of W^{5+} found in sub-stoichiometric WO_3.[57] W^{5+} originates from unsaturated W–O bonding on WO_3 nanorods, and the existence of W^{5+} shows the disintegration of bulk WO_3.[58] The measured spin–orbit separation between W $4f_{5/2}$ and W $4f_{7/2}$ is measured to be 2.2 eV.[59] The slight asymmetry observed in the peaks from the XPS analysis of the δ-MnO_2/WO_3

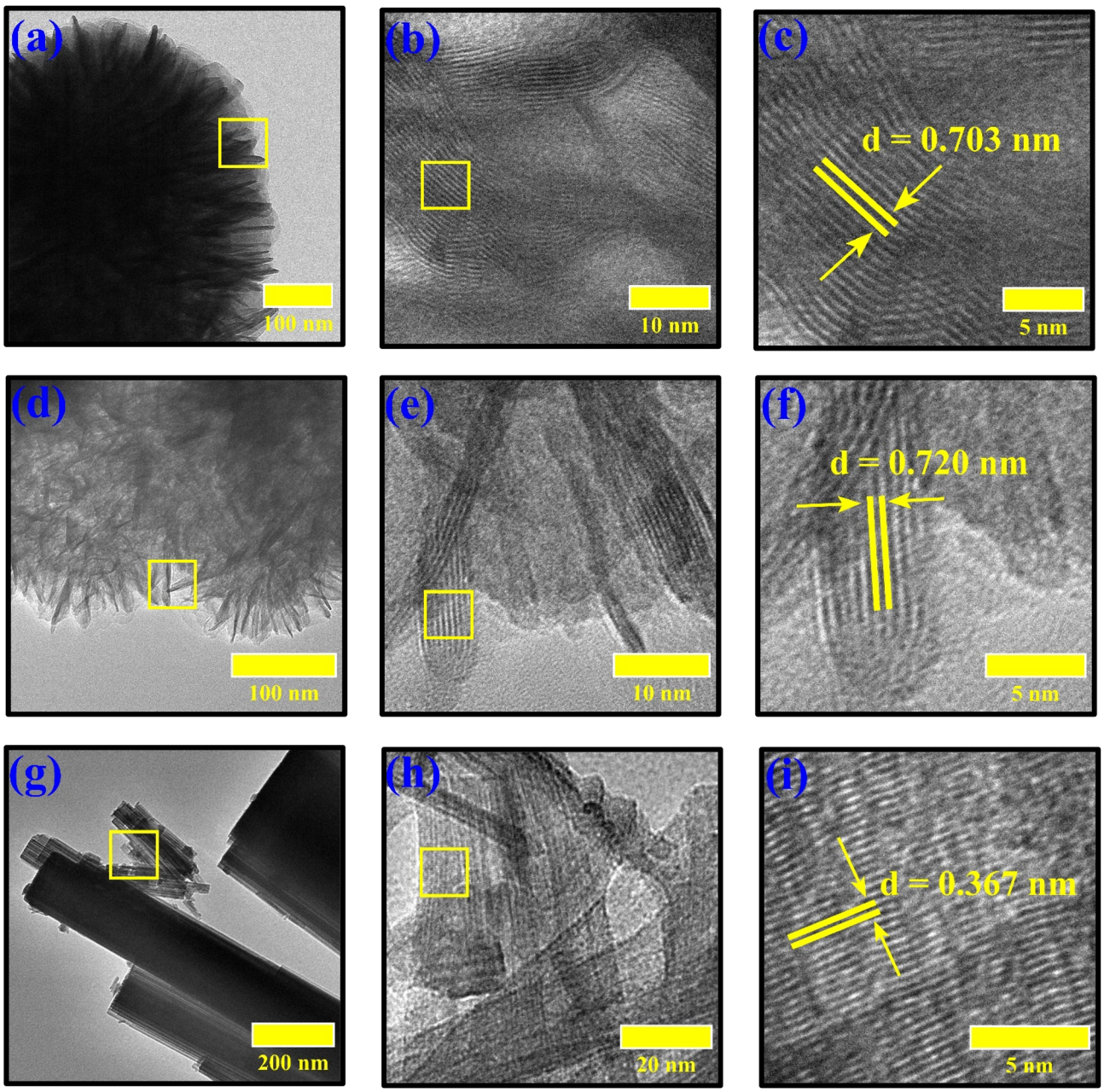

Fig. 4 TEM and HRTEM images showing the internal structure and crystallinity: (a–c) MnO_2 nanoflowers with 0.703 nm spacing; (d–f) MnO_2/WO_3 composite with 0.720 nm lattice fringes; (g–i) WO_3 nanorods with 0.367 nm interplanar spacing.

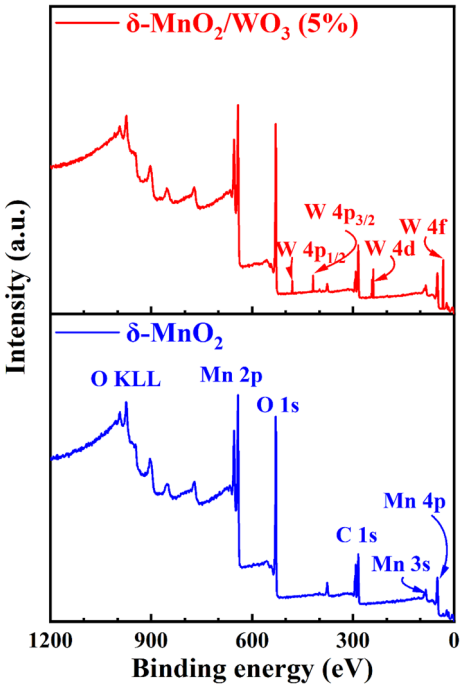

Fig. 5 XPS survey spectra of pristine δ-MnO_2 and δ-MnO_2/WO_3 (5%) show Mn, O, and W elements. Peaks for Mn 2p, O 1s, O KLL auger, and W levels confirm WO_3's incorporation into MnO_2.

nanocomposite suggests electronic connections between δ-MnO_2 and WO_3, supporting the existence of a successful heterojunction interface and improved photocatalytic activity of δ-MnO_2/WO_3 nanocomposite.

3.4. Optical properties

The light-absorption characteristics of δ-MnO_2, WO_3, and their δ-MnO_2/WO_3 (5%) nanocomposites were analyzed using UV-Vis diffuse reflectance spectroscopy (DRS). The variation in absorption behavior results from how the diffused reflected intensity depends on the sample's optical properties, particle size distribution, and filling factor.[60] Fig. 8(a) shows the diffuse reflectance spectra of δ-MnO_2, WO_3, and δ-MnO_2/WO_3 (5%) samples, which indicates that δ-MnO_2 exhibits significant broad reflection across the UV to visible and slightly NIR regions. WO_3 shows an absorption edge at 464 nm, but shows reduced photo response across the visible spectrum.[61] When δ-MnO_2 and WO_3 are combined, the reflectance edges of δ-MnO_2/WO_3 (5%) show broad tails that suggest improved absorption of visible light.[42,53] The optical band gap (E_g) of the samples was calculated from UV-Vis diffuse reflectance spectra using the Kubelka–Munk theory. The spectrum was recorded in diffuse reflectance mode (R) and converted to the Kubelka–Munk function $F(R)$ to remove the scattering component, thereby isolating the absorption behavior. Fig. 8(b) shows the Tauc plot, which is a $(h\nu \times F(R))^n$ *vs.* $(h\nu)$ plot, with $n = 2$ for the direct band gap, h being Planck's constant and ν the frequency. The direct bandgap of the prepared sample was determined by extrapolating the linear region of the curves to $(h\nu \times F(R))^2 = 0$, the ordinate, providing the direct band gap of the samples.[62,63]

The enhanced light absorption of the δ-MnO_2/WO_3 (5%) composite originates from the narrow band gap of δ-MnO_2 and the interaction between δ-MnO_2 and WO_3. This enhanced optical response can be attributed to improved light harvesting and multiple-scattering effects arising from the composite structure, as well as to electronic interactions at the δ-MnO_2/WO_3 interface. The creation of a heterojunction enhances the effective separation and movement of photogenerated charge carriers, which may reduce electron–hole recombination and boosts photocatalytic performance more than pure δ-MnO_2 and WO_3.

Band-edge potential coefficients for WO_3 and δ-MnO_2 semiconductors can be derived from their respective bandgap energies (E_g) using energy-band theory.[64] To investigate the photocatalytic activity of δ-MnO_2 and WO_3, it is essential to determine their respective valence-band maximum (VBM) and conduction-band minimum (CBM). The CBM can be calculated using the empirical equation derived from the Mulliken electronegativity method:

$$E_{CBM} = \chi_s - E^e - \frac{1}{2}E_g \quad (5)$$

$$E_{VBM} = E_{CBM} + E_g \quad (6)$$

Where E_{CBM} is the maximum potential of the conduction band (CB), χ_s is the Mulliken electronegativity, which is the geometric mean of electronegativities, and the value of χ_s depends on the first ionization potential (FIP) and electron affinity (EA), E_g the indirect band gap, which is determined from the Tauc plot and E^e is the free electron energy (4.5 eV). The value of χ_s may be calculated from the following equation:[65]

$$\chi_s = \sqrt[N]{\chi_1^a \chi_2^b \cdots \chi_{n-1}^p \chi_n^q} \quad (7)$$

where χ_n is the electronegativity of a specific atom, q is the mole fraction, and N represents the total number of elements in the compound. Electronegativity of a particular element is calculated as the average of its first ionization potential and its electron affinity, as shown in the equation (Table 2).[66]

$$\chi_n = \frac{\text{FIP} + \text{EA}}{2} \quad (8)$$

The absolute electronegativity (χ) values of MnO_2 and WO_3 were calculated using eqn (7), and the calculations are provided in the SI. The calculated χ values are 5.68 eV for MnO_2 and 6.58 eV for WO_3. Based on these values, the conduction band minimum (E_{CBM}) and valence band maximum (E_{VBM}) of MnO_2 were determined to be 0.65 eV and 1.71 eV, respectively, while those of WO_3 were calculated as 0.62 eV and 3.55 eV. These values are represented on an energy band diagram (Fig. 13), where the vertical axis shows the potential relative to a standard hydrogen electrode (NHE).

3.5. Photocatalytic degradation of metronidazole (MNZ)

3.5.1. Effect of pH on MNZ photodegradation over δ-MnO_2.

The photocatalytic activity is affected by the pH of the solution, which alters the photocatalyst's surface charge, the MNZ state,

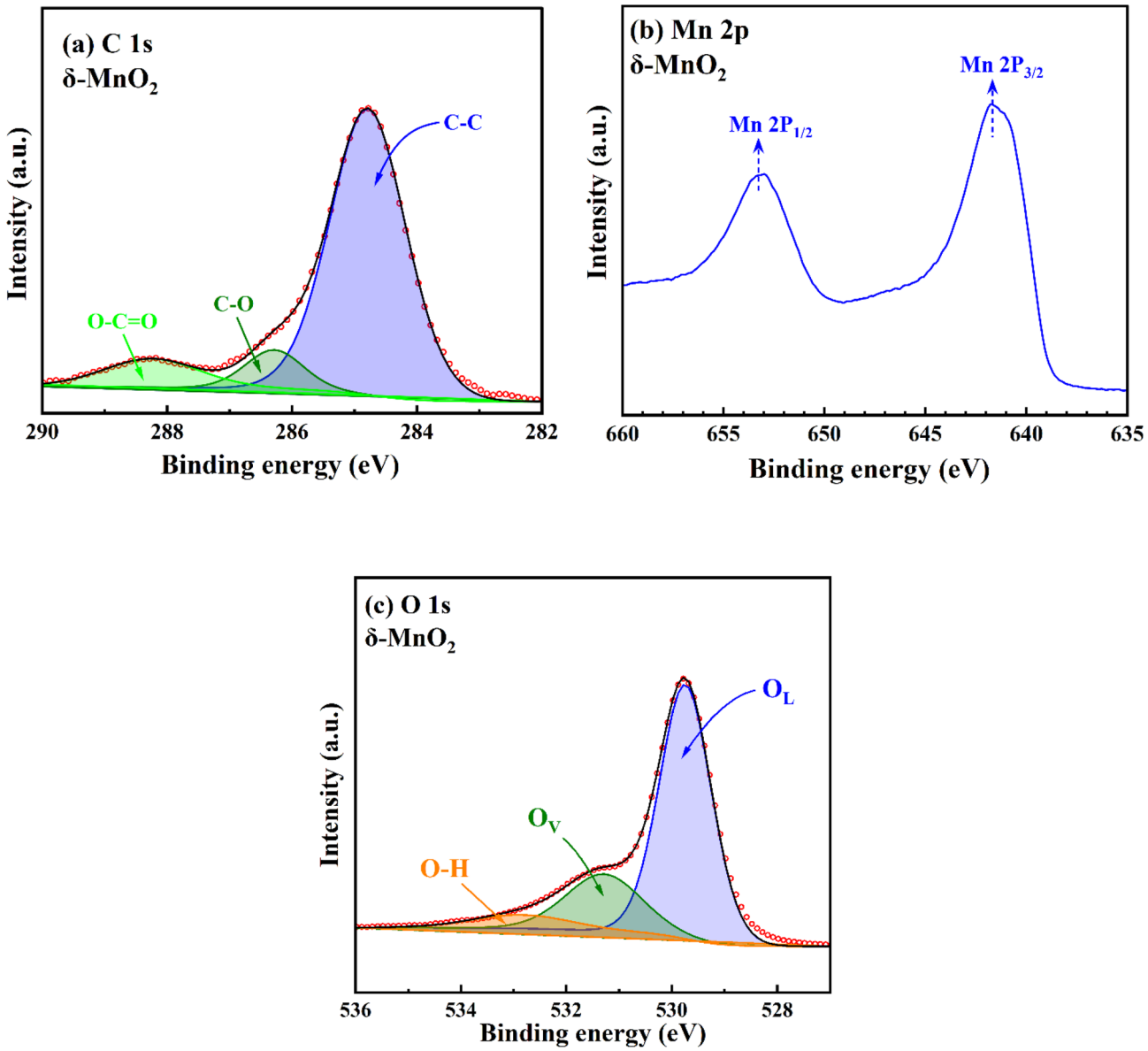

Fig. 6 High-resolution XPS spectra of pure δ-MnO_2 include: (a) the C 1s spectrum, which has been deconvoluted into C–C, C–O, and O–C=O components; (b) the Mn 2p spectrum, displaying the characteristic Mn $2p_{3/2}$ and Mn $2p_{1/2}$ peaks; and (c) the O 1s spectrum, separated into lattice oxygen (O_L), oxygen vacancies (O_V), and surface hydroxyl (O–H) species.

and the generation of reactive oxygen species.[68] At different pH values, electrostatic interactions between MNZ molecules and the δ-MnO_2/WO_3 (5%) surface vary, thereby affecting adsorption behavior and subsequent photocatalytic reactions. Enhanced contact between MNZ and the δ-MnO_2/WO_3 (5%) surface may increase the degradation efficiency. Fig. 9(a and b) shows the effect of pH on MNZ degradation with pure δ-MnO_2, while S2 includes the UV-vis absorption spectra over time. The removal efficiency of MNZ using δ-MnO_2 was 12.07%, 25.04%, 70.09%, and 57.30% at pH 5, 10, 11, and 12, respectively, indicating a clear enhancement in photocatalytic performance under alkaline conditions, with an optimum at pH 11. The higher pseudo-first-order rate constant obtained at pH 11 (0.01104 min^{-1}) suggests that the alkaline conditions promote faster reaction kinetics. At higher pH (pH 12), a slight decrease in degradation efficiency was observed, which may be attributed to the increased electrostatic repulsion or scavenging effects that limit the availability of reactive radicals.

3.5.2. Effect of pH on MNZ photodegradation over WO_3. For pure WO_3, a similar trend has been observed: alkaline solutions facilitate MNZ degradation (Fig. 10(a and b)). The improved performance at higher pH values is mainly due to the increased availability of OH^- ions, which facilitate the generation of highly reactive hydroxyl radicals ($OH^•$). In contrast, the acidic pH suppresses the formation of $OH^•$ by increasing the concentration of H^+ ions, thereby reducing photocatalytic efficiency. The S4 displays the UV-vis absorption spectra of MNZ at various pH levels. Previous studies have reported similar

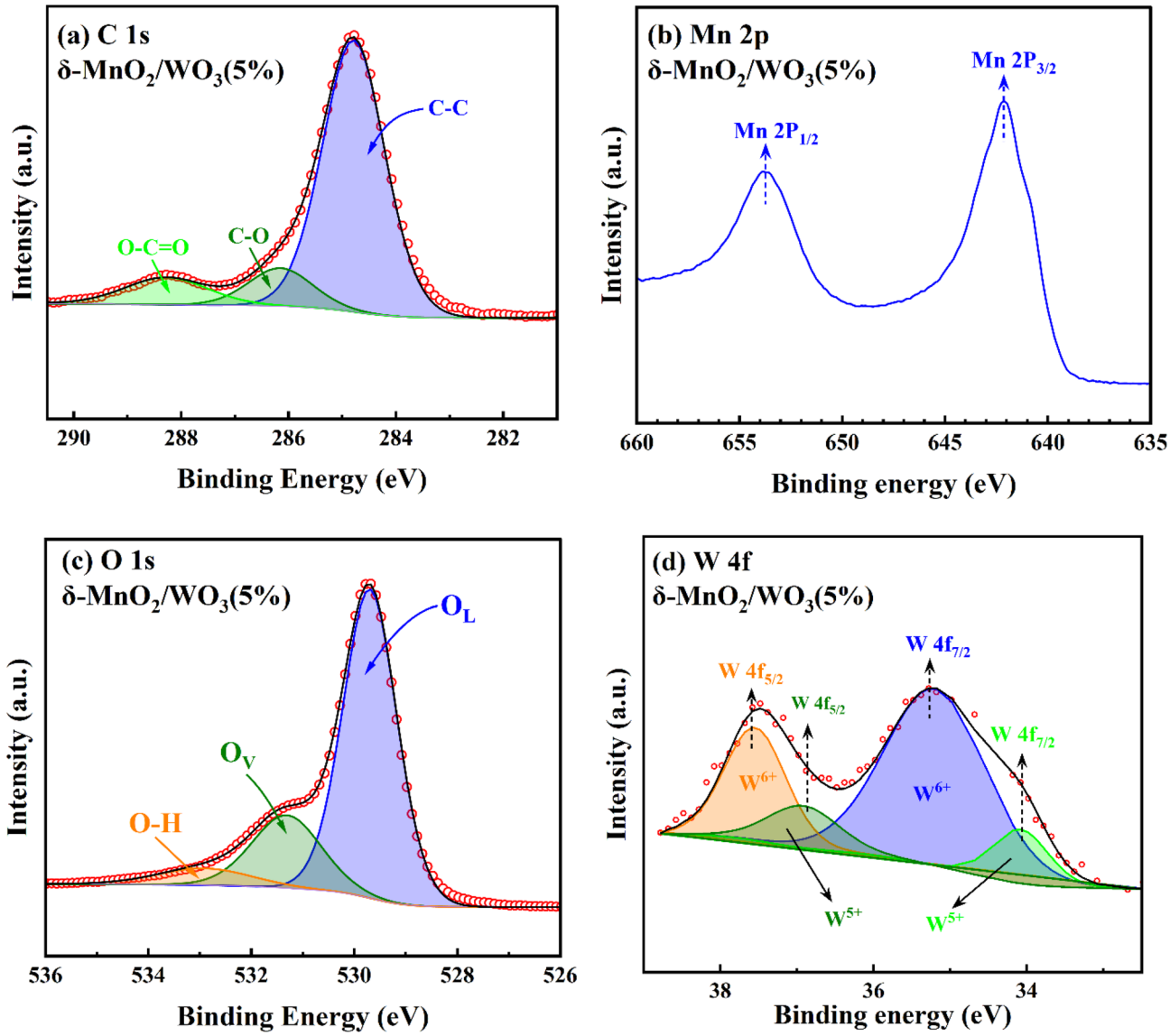

Fig. 7 High-resolution XPS spectra of the δ-MnO_2/WO_3 (5%) heterojunction composite include: (a) the C 1s spectrum deconvoluted into C–C, C–O, and O–C=O components; (b) the Mn 2p spectrum showing Mn $2p_{3/2}$ and Mn $2p_{1/2}$ peaks; (c) the O 1s spectrum featuring lattice oxygen (O_L), oxygen vacancies (O_V), and surface hydroxyl groups (O–H); and (d) the W 4f spectrum indicating W $4f_{7/2}$ and W $4f_{5/2}$ peaks associated with W^{6+} and W^{5+} oxidation states.

findings for higher MNZ degradation in alkaline media.[69,70] Tran *et al.* found that a pH of 10 was optimal for the photodegradation of MNZ using a pure ZnO catalyst under UV-C irradiation (100 W), which is significantly higher than the typical near-neutral pH of contaminated water.[71] Although the highest degradation efficiency for both δ-MnO_2 and $WO_3$was achieved at pH 11, the photocatalytic activity was systematically studied across a broad pH range (5–12), covering acidic and highly alkaline conditions. It is important to note that real wastewater typically has a near-neutral pH (6–8), and operating at a strongly alkaline pH may require chemical adjustments and subsequent neutralization, which can increase operational costs. Future research may aim to improve catalyst performance under near-neutral pH to increase practical applicability.

3.5.3. Effect of δ-MnO_2 dosage on MNZ photodegradation. The effect of δ-MnO_2 dose on MNZ degradation is seen in Fig. 11(a and b). Increasing the photocatalyst dose correlated with higher MNZ photodegradation yield. At a photocatalyst dose of 0.5 g L^{-1} in the initial solution at pH 11, the yield of MNZ photodegradation reached 70.09% (Fig. 11b). Raising the photocatalyst dose increases the number of active sites, leading to greater free-radical production and enhanced MNZ degradation.[72] The observation is clear: adding more δ-MnO_2 photocatalyst results in increased adsorption of MNZ molecules on the surface and simultaneously boosts the production of photoinduced electrons and holes in the solution. These photoinduced electrons and holes interact with dissolved oxygen and water on the δ-MnO_2 surface, producing additional

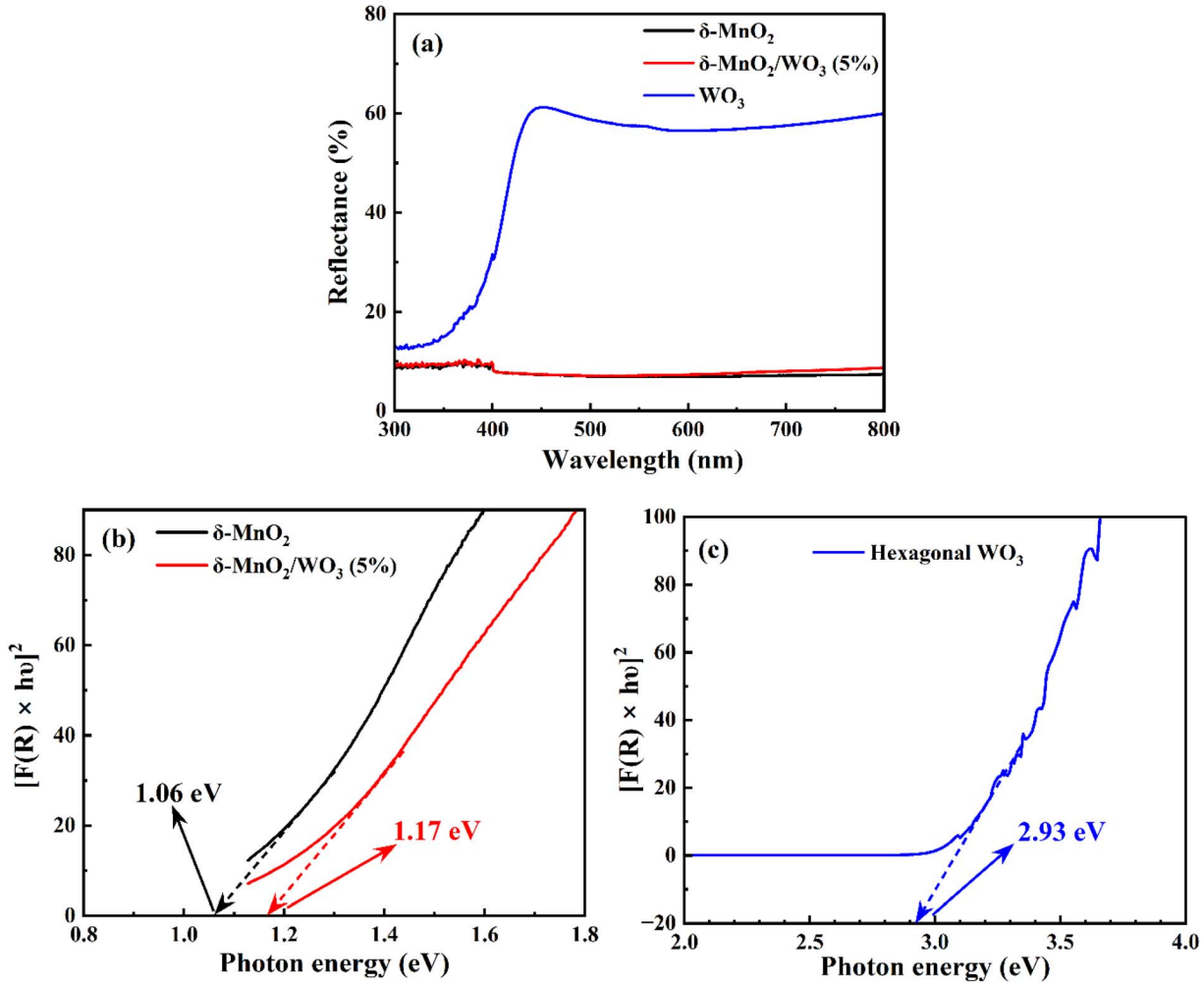

Fig. 8 (a) Diffuse reflectance spectra (DRS) for pure δ-MnO_2, WO_3, and the δ-MnO_2/WO_3 (5%) nanocomposite. (b) Tauc plots $(F(R)h\nu)^2$ *vs.* photon energy for δ-MnO_2 and δ-MnO_2/WO_3 (5%), indicating an optical band gap of 1.06 eV for MnO_2 and 1.17 eV after forming a composite with WO_3. (c) Tauc plot of hexagonal WO_3, yielding an optical band gap of approximately 2.93 eV.

Table 2 First ionization potential (FIP), electron affinity (EA), and electronegativity (χ_n) of atoms

Atoms	FIP (eV)	EA (eV)	χ_n
Mn	7.434	−0.97 (ref. 67)	3.232
W	7.980	0.817	4.399
O	13.618	1.461	7.5395

reactive $OH^{\bullet}$ species, which further degrade MNZ.[72–74] However, a further increase in the δ-MnO_2 dosage from 0.5 to 0.6 g L^{-1} resulted in a lower photocatalytic efficiency. This decrease is mainly caused by the photocatalyst aggregation, which reduces the active surface area for degradation, and by excessive catalyst loading, which diminishes light penetration by increasing suspension turbidity and photon scattering.[75–77] The results align well with earlier studies, which also observed an initial increase in photocatalytic performance that later declined at higher catalyst concentrations.[77,78]

3.5.4. Photocatalytic performance of δ-MnO_2/WO_3 composite. To evaluate the photocatalytic performance of the composite, the degradation efficiency of the δ-MnO_2/WO_3 (5%) composite was compared with that of Pure δ-MnO_2 and WO_3. As indicated in Fig. 12(a and b), the photocatalytic performance of δ-MnO_2/WO_3 (5%) composite was significantly higher than that of individual components, showing the beneficial role of interfacial coupling between δ-MnO_2 and WO_3.

As discussed in the earlier sections, both δ-MnO_2 and WO_3 showed the highest degradation efficiency at pH 11. So pH 11 was considered optimal and used in the subsequent experiment for the composite. In addition, the photocatalyst dosage was fixed at 0.5 g L^{-1}, which was identified as the optimal concentration for δ-MnO_2 during the catalyst optimization studies. Under these optimized conditions, δ-MnO_2/WO_3 (5%) showed the highest degradation efficiency. The higher degradation efficiency of the δ-MnO_2/WO_3 (5%) composite can be attributed to the hierarchical δ-MnO_2 nanoflower–WO_3 nanorod structure, which may enhance adsorption capacity, and to the effective separation and migration of photogenerated charge carriers

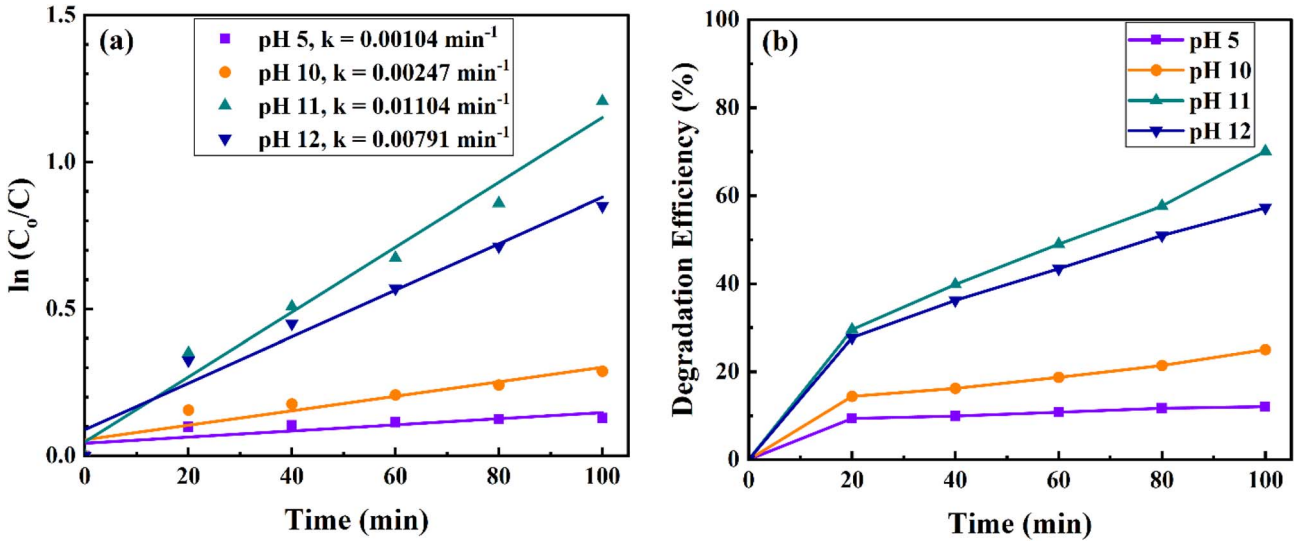

Fig. 9 (a) Pseudo-first-order kinetic plots of $\ln(C_0/C)$ *versus* irradiation time and (b) corresponding degradation efficiency *versus* irradiation time for the photocatalytic degradation of MNZ over pristine MnO_2 at different solution pH values (pH 5, 10, 11, and 12). The MnO_2 dose was maintained at 0.5 g L^{-1}, with an initial MNZ concentration of 10 ppm.

across the heterojunction. The interaction between δ-MnO_2 and WO_3 can facilitate targeted charge transfer and reduce electron–hole pair recombination, as will be elaborated upon later.

The stability and reusability of the δ-MnO_2/WO_3 (5%) composite were evaluated through five consecutive photocatalytic cycles under identical conditions (80 min irradiation per cycle). As shown in Fig. S6, the degradation efficiency decreased slightly from 73.51% in the first cycle to approximately 70% in the fifth cycle, indicating good structural stability and sustained photocatalytic activity. To further verify the structural stability after cycling, XPS analysis was performed on the reused catalyst. The Mn 2p spectra before and after the recyclability test (Fig. S6) show no significant shift in binding energy or change in oxidation state, confirming that the chemical structure of the composite remains stable during repeated photocatalytic operation.

3.5.5. Kinetics of metronidazole degradation. For all catalysts, the decrease in MNZ concentration over time exhibited a consistent trend, enabling the degradation process to be analyzed using a kinetic model. The degradation kinetics were analyzed using the pseudo-first-order model (pseudo-first-order fitting parameters are tabulated in Table S1). In heterogeneous photocatalysis, this model is commonly derived from the Langmuir–Hinshelwood (L–H) mechanism under low initial

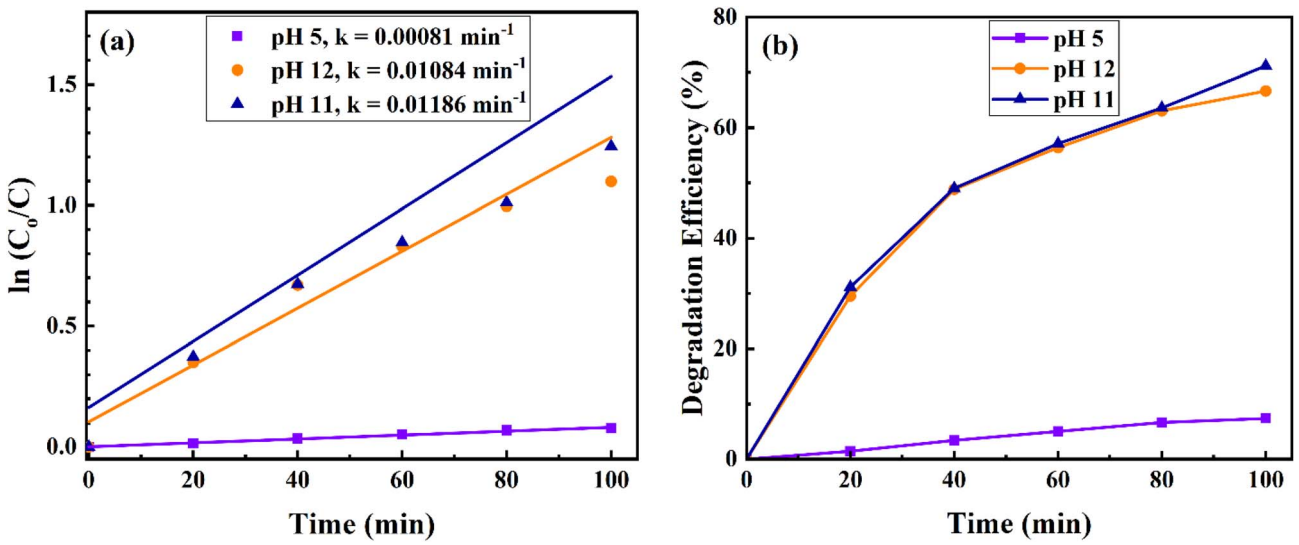

Fig. 10 (a) Evolution of $\ln(C_0/C)$ with irradiation time during the photocatalytic degradation of MNZ using pristine WO_3 at different solution pH values (pH 5, 11, and 12). (b) Corresponding MNZ degradation efficiency *versus* irradiation time for the same pH conditions. The initial MNZ concentration was kept at 10 ppm, and the WO_3 dosage was kept constant (0.5 g L^{-1}) throughout the experiments.

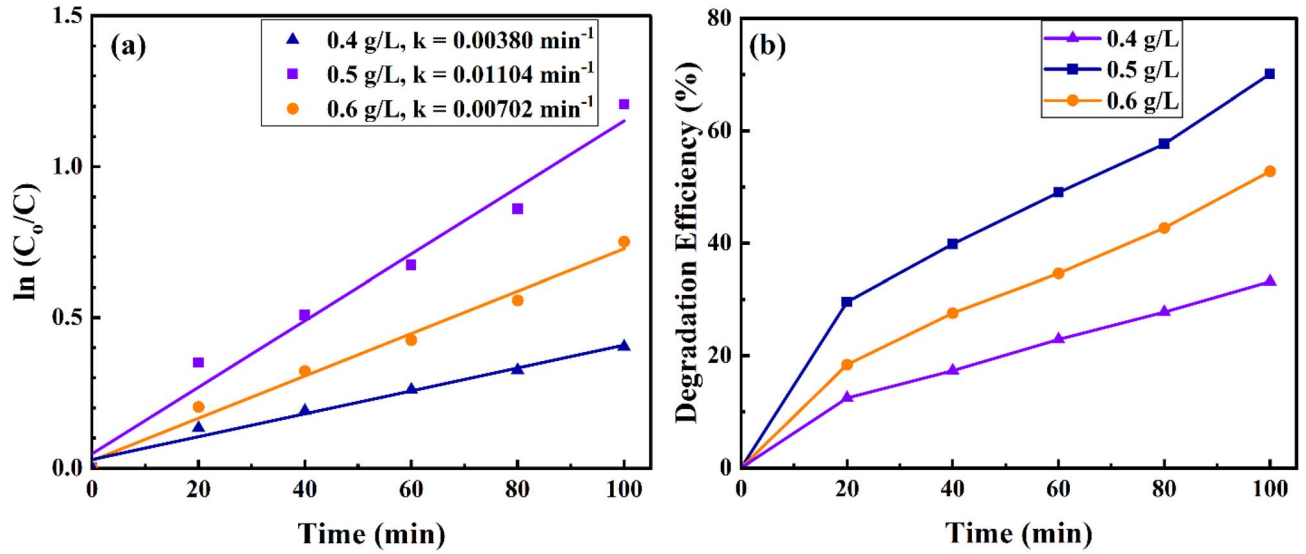

Fig. 11 (a) Time-dependent $\ln(C_0/C)$ profiles obtained during the photocatalytic degradation of MNZ using pure δ-MnO_2 at different catalyst loadings (0.4, 0.5, and 0.6 g L^{-1}) under UV irradiation, showing pseudo-first-order kinetic behavior. (b) Corresponding MNZ degradation efficiency over time at different δ-MnO_2 loadings. The initial MNZ concentration was 10 ppm, with the solution pH maintained at 11.

pollutant concentrations, where the surface adsorption term is constant, and the rate expression simplifies to an apparent first-order form. Since the initial metronidazole concentration in this study was relatively low (10 ppm), the pseudo-first-order approximation is considered appropriate. The degradation kinetics were examined by plotting $\ln(C_0/C)$ against irradiation time, following the equation $\ln(C_0/C) = -kt$, where C_0 represents the initial concentration, C is the concentration at time t, and k is the apparent rate constant.[79,80] The pseudo-first order rate constants (k) for pure δ-MnO_2, pure WO_3, and the δ-MnO_2/WO_3 heterojunction are compared and displayed in Fig. 12, with δ-MnO_2/WO_3 (5%) showing the highest rate constant of 0.01541 min^{-1}. The findings clearly indicate that, among all samples, the δ-MnO_2/WO_3 (5%) composite significantly enhanced MnO_2's photocatalytic activity for MNZ degradation.

The enhanced photocatalytic performance of the MnO_2/WO_3 composite compared to the pure materials may be attributed primarily to the formation of a heterojunction interface between MnO_2 and WO_3. The interfacial contact facilitates efficient charge separation and suppresses electron–hole recombination. Unlike studies where varying component ratios lead to surface coverage effects and reduced activity, the present

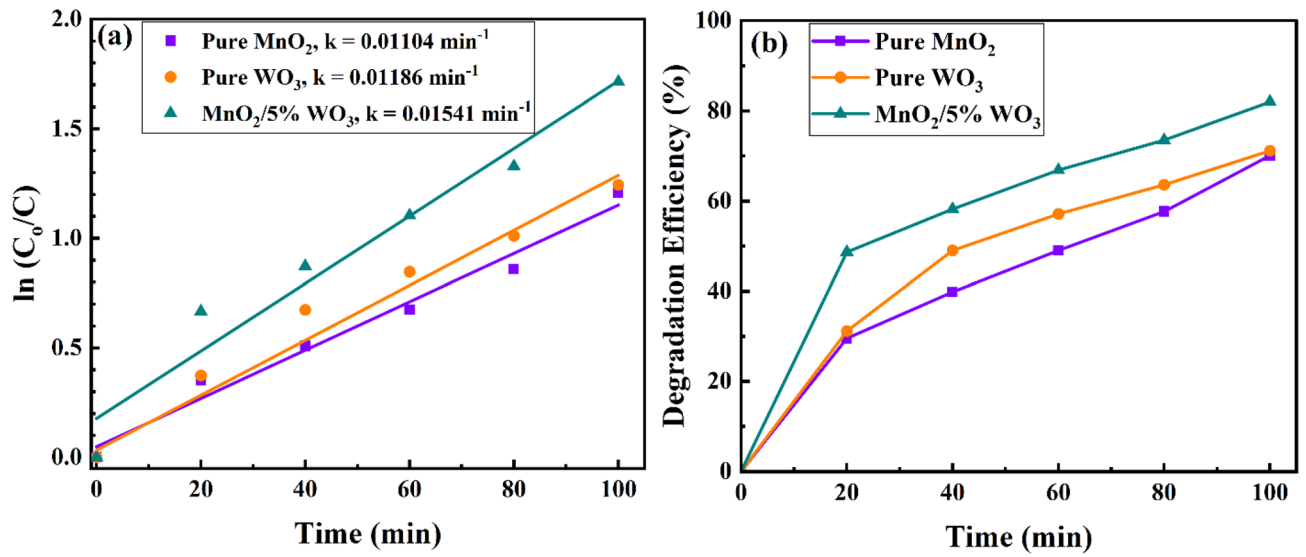

Fig. 12 (a) Pseudo-first-order kinetic plots are shown by plotting $\ln(C_0/C)$ against irradiation time during the photocatalytic degradation of metronidazole (MNZ) using pristine δ-MnO_2, pristine WO_3, and δ-MnO_2/WO_3 (5%) under identical experimental conditions. (b) Corresponding MNZ degradation efficiency *vs.* irradiation time for the same set of photocatalysts.

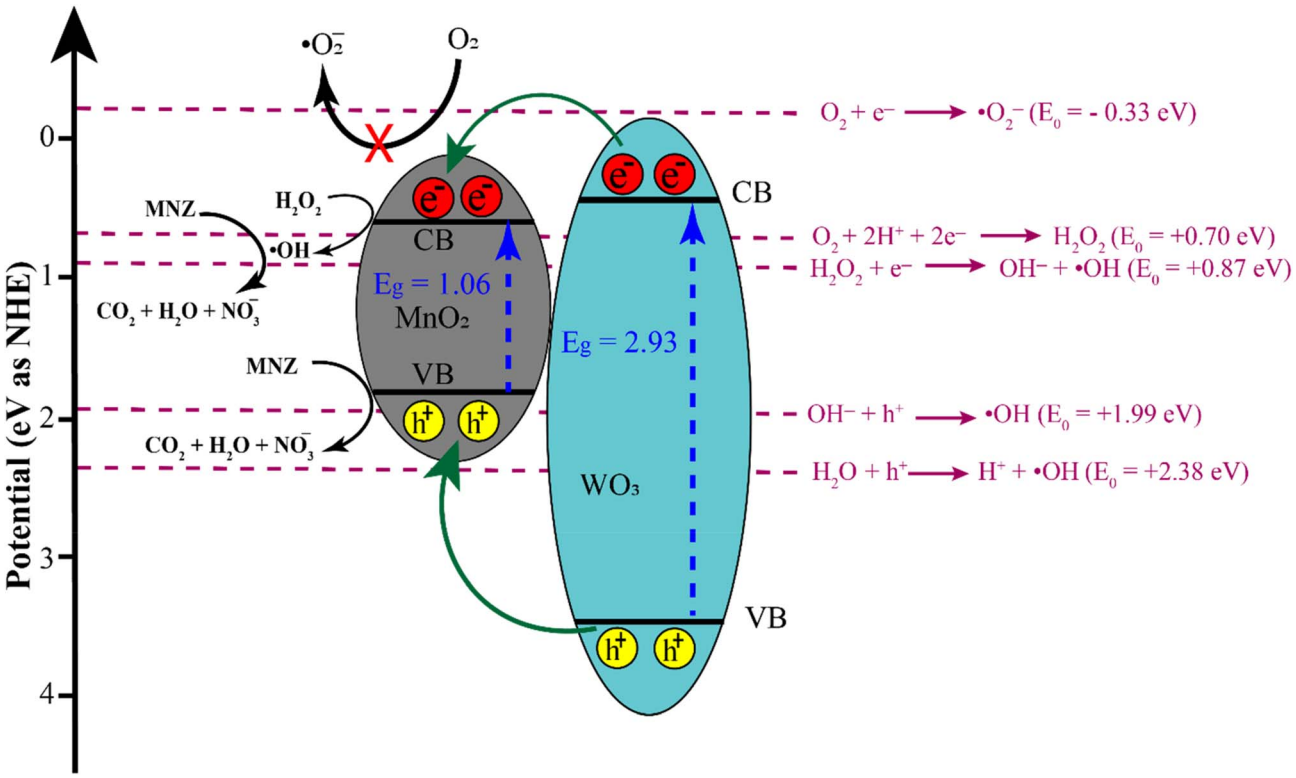

Fig. 13 Band-edge alignment and proposed Type-I charge-transfer mechanism in the δ-MnO_2/WO_3 (5%) nano-heterojunction, referenced to the NHE scale.

work focuses on a single optimized heterojunction composition.

3.5.6. Possible mechanism of mixed semiconductor photocatalyst. The improved photocatalytic performance of the δ-MnO_2/WO_3 (5%) system mainly stems from better separation and transfer of photogenerated charge carriers, facilitated by the formation of a heterojunction between δ-MnO_2 and WO_3. This optimizes the separation and transfer rates of photo-induced electron–hole pairs, greatly enhancing photocatalytic performance.[81] When UV light irradiates the photocatalyst, electrons are excited from the valence bands to the conduction bands of both materials, due to their suitable band gaps, while holes are simultaneously generated in their valence bands. The calculated band alignment suggests the formation of a Type-I

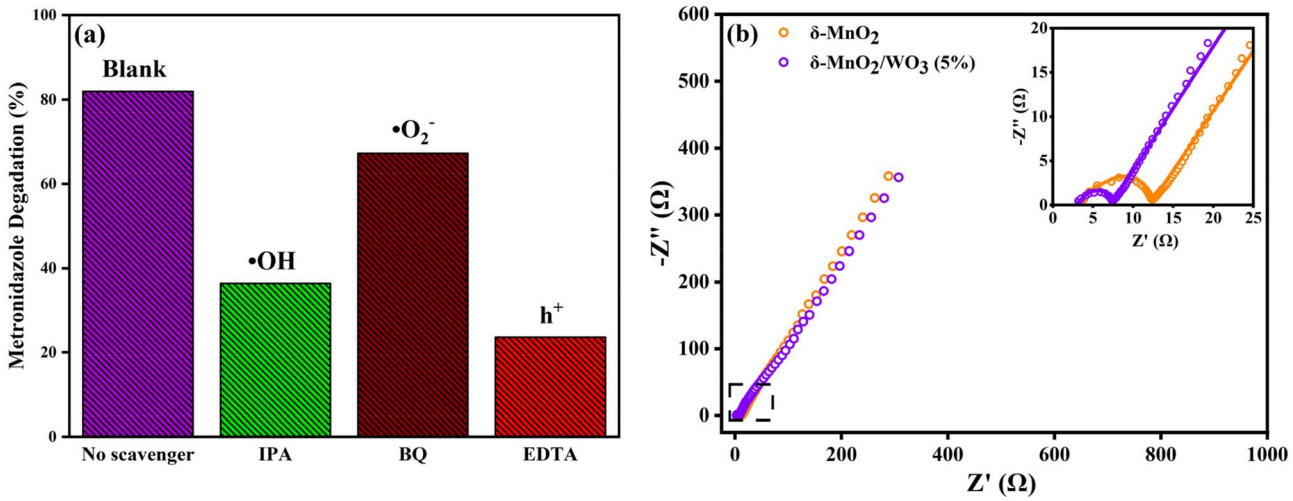

Fig. 14 (a) Radical scavenger test for reactive radical during photocatalytic degradation of metronidazole. (b) EIS Nyquist plots of pure δ-MnO_2 and δ-MnO_2/WO_3 (5%) composite.

Table 3 Comparison of the photocatalytic degradation efficiency of δ-MnO_2/WO_3 (5%)

Photocatalyst	Target pollutant	Irradiation source	Pollutant concentration (mg L^{-1})	Photocatalyst dosage	Time (min)	Photocatalytic efficiency (%)	Ref.
$ZnO/ZnAl_2O_4$	Metronidazole	Solar light	20	40 mg/100 mL	120	50	92
CuO	Metronidazole	UV light	1–8	20 mg/100 mL	120	85	93
ZnO	Metronidazole	UV light	80	150 mg/100 mL	180	96.55	94
CuS/NiS	Metronidazole	Visible light	150	20 mg/100 mL	120	23.3	95
$MnWO_4/Bi_2S_3$	Metronidazole	150 W Xe visible light	20	120 mg/100 mL	180	83.3	96
MnO_2/WO_3	Metronidazole	6 W Xe UV lamp	10	50 mg/100 mL	100	82	This work

heterojunction between δ-MnO_2 and WO_3. When exposed to light, electron–hole pairs form in both semiconductors. Due to the relative positions, photogenerated electrons in the CB of WO_3 tend to transfer to the CB of MnO_2, while holes in the VB of WO_3 migrate toward the VB of MnO_2.[82] This carrier redistribution leads to spatial confinement of charge carriers within MnO_2, thereby suppressing recombination *via* interfacial charge transfer and improving photocatalytic performance, which is shown in Fig. 13.

The photogenerated electron accumulated on MnO_2 can reduce dissolved O_2 into H_2O_2 and H_2O_2 can subsequently be converted into $^{\bullet}OH$ through electron assisted reduction.[83,84] The conduction band edge potential of MnO_2 exceeds the standard redox potential of $O_2/^{\bullet}O_2^-$ (−0.33 eV),[85] which indicates that the electrons in the conduction band of MnO_2 are unable to reduce O_2 to the superoxide radical ion ($^{\bullet}O_2^-$). The photogenerated holes transferred to the VB of MnO_2 have sufficient energy to directly degrade metronidazole. The generated charge carriers facilitate the photocatalytic degradation of pollutants, while heterojunction formation enhances the separation of photogenerated charge carriers, thereby improving photocatalytic activity. The primary reaction steps in this mechanism under UV light irradiation are summarized as follows:

$$(MnO_2/WO_3) + h\nu \rightarrow (MnO_2/WO_3)\, e_{CB}^- + (MnO_2/WO_3)\, h_{VB}^+ \quad (9)$$

$$e_{CB}^-(WO_3) \xrightarrow{\text{transfer}} e_{CB}^-(MnO_2) \quad (10)$$

$$2e_{CB}^-(MnO_2) + O_2 + 2H^+ \rightarrow H_2O_2 \quad (11)$$

$$H_2O_2 + e_{CB}^-(MnO_2) \rightarrow OH^- + {}^{\bullet}OH \quad (12)$$

$$h_{VB}^+(WO_3) \xrightarrow{\text{transfer}} h_{VB}^+(MnO_2) \quad (13)$$

$$h_{VB}^+(MnO_2) + \text{metronidazole} \rightarrow \text{intermediate} \rightarrow CO_2 + H_2O + NO_3^- \quad (14)$$

$$^{\bullet}OH + \text{metronidazole} \rightarrow \text{intermediate} \rightarrow CO_2 + H_2O + NO_3^- \quad (15)$$

It should be noted that the present band alignment analysis is based on the Mulliken electronegativity method, which provides an approximate estimation of band positions. Experimental techniques such as valence band XPS and Mott–Schottky analysis can provide deeper insight into charge-transfer behavior and heterojunction type, as demonstrated in studies of electrochemical characterization of semiconductor systems.[86]

The effectiveness of charge separation at the interface for photogenerated electrons (e^-) and holes (h^+) is considered a key factor in photocatalytic performance.[87] As shown in Fig. 14(a) the degradation efficiency dramatically dropped at 23.63% in the presence of EDTA suggesting that photogenerated h^+ play a dominant role in the degradation of metronidazole. Additionally, metronidazole degradation was noted 36.40% with IPA, indicating that $^{\bullet}OH$ radicals constitute significant reactive species. But addition of BQ resulted in a comparatively slight drop in degradation efficiency (67.27%), suggesting a minimal contribution from reactive species associated to $^{\bullet}O_2^-$. These findings show that h^+ and $^{\bullet}OH$ primarily control photocatalytic degradation of metronidazole while $^{\bullet}O_2^-$ playing a minor role. To gain insight into light-induced charge-transfer dynamics and the interface charge-transfer rate, electrochemical impedance spectroscopy (EIS) was performed.[80] The EIS technique effectively investigates the fundamental mechanisms of charge transfer.[88] The semicircle in the high-to-medium frequency range represents the charge-transfer resistance (R_{ct}) and the double-layer capacitance at the electrode/electrolyte interface. The Nyquist plots for δ-MnO_2 and δ-MnO_2/WO_3 (5%) are shown in Fig. 14(b), where the smallest semicircle diameters for δ-MnO_2/WO_3 (5%) indicate lower charge-transfer resistance and improved charge separation efficiency. This would improve electron diffusion and boost the transfer rate, facilitating greater involvement of electrons and holes in the photocatalytic process.[85] The EIS results indicate that the recombination of light-induced carriers is significantly suppressed by the formation of the δ-MnO_2/WO_3 (5%) heterojunction, thereby improving photocatalytic activity. Zhang *et al.*[85] and related studies on MnO_2-based heterojunctions[89–91] have reported significant improvement in photocatalytic activity attributed to improved interfacial charge transfer. The results suggest that the rate of separation of photogenerated electron–hole pairs increased upon combining MnO_2 with WO_3, with δ-MnO_2/WO_3 (5%) exhibiting the highest photo charge-separation efficiency.

The photocatalytic efficiency of the developed δ-MnO_2/WO_3 (5%) heterojunction was compared with that of previously reported photocatalysts for the photodegradation of MNZ. The results presented in Table 3 indicate that the synthesized δ-MnO_2/WO_3 (5%) heterojunction exhibited photocatalytic performance that is comparable to that reported in the literature. The fabricated photocatalyst shows potential for

environmental remediation, particularly for the treatment of pharmaceuticals, antibiotics, and organic dyes. Although the reactive species were proposed based on band-structure analysis and established photocatalytic mechanisms, radical-trapping or ESR experiments were not conducted in the present study. Future investigations may include scavenger-based and spectroscopic analyses to experimentally verify the dominant active species.

4. Conclusion

This work demonstrates the fabrication and performance of a structurally coherent binary δ-MnO_2/WO_3 type-I heterojunction photocatalyst with an increased number of active sites and improved light-harvesting potentials. XRD, FESEM/TEM, and SAED confirmed the successful incorporation of WO_3 into δ-MnO_2 without creating any impurity phases. XPS revealed oxygen vacancies and the presence of W^{5+}, which are beneficial for charge separation and surface reactivity. Under UV light, the δ-MnO_2/WO_3 (5%) composite evidently exhibited higher MNZ degradation efficiency and a larger pseudo-first-order rate constant. Electrochemical impedance spectroscopy further indicated that the heterojunction substantially suppresses recombination. The formation of a type-I heterojunction preserves strongly oxidizing holes in WO_3 and high-energy electrons in δ-MnO_2. The δ-MnO_2/WO_3 (5%) system outperforms several reported UV-active MNZ photocatalysts when normalized by irradiation time, pollutant concentration, and catalyst dosage, emphasizing its potential for practical, cost-effective water treatment applications.

Author contributions

The manuscript was written through the contributions of all authors. All authors have given approval to the final version of the manuscript. Md Shafayatul Islam: conceptualization, methodology, investigation, formal analysis, writing – original draft. Mehedi Hasan Prince: methodology, formal analysis, writing – review & editing. Koushik Roy Chowdhury: investigation, formal analysis, writing – review & editing. Sifat Sharmin Rawfa: investigation, formal analysis, writing – review & editing. Ilma Jahan Ritu: formal analysis, writing – review & editing. S. M. Khalid Hossain: formal analysis, writing – review & editing. Ahmed Sharif: conceptualization, resources allocation, supervision, writing – review & editing.

Conflicts of interest

There are no conflicts of interest to declare.

Data availability

All data supporting the findings of this study are available within the article and its supplementary information (SI). Supplementary information is available. See DOI: https://doi.org/10.1039/d6ra00866f.

Acknowledgements

This research did not receive any specific grant from funding agencies in the public, commercial, or non-profit sectors. The authors would like to express their gratitude to the Basic Research Grant of the Bangladesh University of Engineering and Technology (BUET). The authors would like to express their gratitude to department of Materials and Metallurgical Engineering, BUET and Materials science division, Atomic Energy Centre, Dhaka, for their assistance with nanoparticles synthesis and characterization.

References

1 A. Al Miad, S. P. Saikat, Md. K. Alam, Md. Sahadat Hossain, N. M. Bahadur and S. Ahmed, *Nanoscale Adv.*, 2024, **6**, 4781–4803.
2 A. Balapure, J. Ray Dutta and R. Ganesan, *RSC Appl. Interfaces*, 2024, **1**, 43–69.
3 A. A. Tessema, C.-M. Wu and K. G. Motora, *ACS Omega*, 2022, **7**, 38475–38486.
4 P. P. Singh, G. Pandey, Y. Murti, J. Gairola, S. Mahajan, H. Kandhari, S. Tivari and V. Srivastava, *RSC Adv.*, 2024, **14**, 20492–20515.
5 F. Bashiri, S. M. Khezri, R. R. Kalantary and B. Kakavandi, *J. Mol. Liq.*, 2020, **314**, 113608.
6 Y.-L. Wang, A. Gómez-Avilés, S. Zhang, J. J. Rodriguez, J. Bedia and C. Belver, *J. Environ. Chem. Eng.*, 2023, **11**, 109744.
7 W. Du, Q. Xu, D. Jin, X. Wang, Y. Shu, L. Kong and X. Hu, *RSC Adv.*, 2018, **8**, 40022–40034.
8 A. Seidmohammadi, Y. Vaziri, A. Dargahi and H. Z. Nasab, *Biomass Convers. Biorefinery*, 2023, **13**, 9057–9073.
9 E. Shabanian-Broujeni and A. Nezamzadeh-Ejhieh, *Heliyon*, 2024, **10**, e31353.
10 F. Tamaddon, M. H. Mosslemin, A. Asadipour, M. A. Gharaghani and A. Nasiri, *Int. J. Biol. Macromol.*, 2020, **154**, 1036–1049.
11 G. Lu, X. Li, P. Lu, H. Guo, Z. Wang, Q. Zhang, Y. Li, W. Sun, J. An and Z. Zhang, *Toxics*, 2024, **12**, 70.
12 Y. Lu, X. Wang, Y. Zhang, S. Ren, Y. Mei and L. Xu, *Catalysts*, 2024, **15**, 3.
13 A. R. Riya, A. Daiyan, M. H. Prince, T. M. Aishi, T. D. Prome, Md. A. Zubair, Md. F. Islam and T. Fakhrul, *RSC Adv.*, 2025, **15**, 38510–38521.
14 M. S. Islam, K. R. Chowdhury, S. M. Hoque and A. Sharif, *Mater. Adv.*, 2024, **5**, 2946–2967.
15 Z. Li, D. Liao, G. Tian, X. Fan, X. Chai, W. Chang, Y. Gao, B. Yuan, Z. Li, F. Wei and C. Zhang, Determination of Mn Valence States in Nanocatalysts During Sustainable Syngas Conversion, *J. Am. Chem. Soc.*, 2025, **147**(36), 32548–32559, DOI: 10.1021/jacs.5c06550.
16 Md. A. H. C. Anik, T. M. A. I. Bin Belal, M. S. Islam, K. R. Chowdhury, M. Brahma, S. I. Mim, A. N. Ahmed and A. Sharif, *Mater. Adv.*, 2025, **6**, 9723–9745.
17 N. S. George, R. M. Cherian, D. A. Nayana, D. R. R, R. T. Subramaniam and A. Aravind, *Chem. Phys. Impact*, 2024, **9**, 100681.

18 S. Das, A. Samanta and S. Jana, *ACS Sustain. Chem. Eng.*, 2017, **5**, 9086–9094.
19 A. Alinda Shaly, G. Hannah Priya, A. Matharasi, A. Surya Prabha and J. Mary Linet, *Mater. Today Proc.*, 2022, **68**, 282–286.
20 Y. Lu, Y. Zhao, S. Wang and B. Hu, Exploring charge-transfer of 2D borophene in carbon nitride: boosting uranium photoreduction, *Desalination*, 2026, **619**, 119488, DOI: 10.1016/j.desal.2025.119488.
21 I. M. Szilágyi, B. Fórizs, O. Rosseler, Á. Szegedi, P. Németh, P. Király, G. Tárkányi, B. Vajna, K. Varga-Josepovits, K. László, A. L. Tóth, P. Baranyai and M. Leskelä, *J. Catal.*, 2012, **294**, 119–127.
22 D. Sánchez Martínez, A. Martínez-de La Cruz and E. López Cuéllar, *Appl. Catal. Gen.*, 2011, **398**, 179–186.
23 G. Lu, X. Li, P. Lu, H. Guo, Z. Wang, Q. Zhang, Y. Li, W. Sun, J. An and Z. Zhang, *Toxics*, 2024, **12**, 70.
24 P. Shandilya, S. Sambyal, R. Sharma, P. Mandyal and B. Fang, *J. Hazard. Mater.*, 2022, **428**, 128218.
25 M. S. Islam, S. M. Hoque, M. Rahaman, M. R. Islam, A. Irfan and A. Sharif, *ACS Omega*, 2024, **9**, 10680–10693.
26 S. Bag and C. R. Raj, *J. Mater. Chem. A*, 2016, **4**, 8384–8394.
27 Y. Song, J. Zhao, Y. Zhao and Z. Huang, *RSC Adv.*, 2016, **6**, 99898–99904.
28 P. Van Tong, N. D. Hoa, N. Van Duy and N. Van Hieu, *RSC Adv.*, 2015, **5**, 25204–25207.
29 M. Abbas, K. Hussain, N. H. Shah, M. Ilyas, R. Batool, M. A. Ahmad, Y. Cui and Y. Wang, *J. Mater. Sci. Technol.*, 2024, **197**, 160–170.
30 I. Vamvasakis, I. Georgaki, D. Vernardou, G. Kenanakis and N. Katsarakis, *J. Sol-Gel Sci. Technol.*, 2015, **76**, 120–128.
31 M. S. Islam, K. R. Chowdhury, S. M. Hoque and A. Sharif, *Mater. Adv.*, 2024, **5**, 2946–2967.
32 A. S. Belousov, E. V. Suleimanov, A. A. Parkhacheva, D. G. Fukina, A. V. Koryagin, A. V. Koroleva, E. V. Zhizhin and A. P. Gorshkov, *Solid State Sci.*, 2022, **132**, 106997.
33 M. H. Prince, T. M. Aishi, Md. A. Zubair and T. Fakhrul, in *2023 IEEE International Conference on Telecommunications and Photonics (ICTP)*, IEEE, Dhaka, Bangladesh, 2023, pp. 01–05.
34 M. S. Islam, S. M. Hoque, M. Rahaman, M. R. Islam, A. Irfan and A. Sharif, *ACS Omega*, 2024, **9**, 10680–10693.
35 A. Goktas, S. Modanlı, A. Tumbul and A. Kilic, *J. Alloys Compd.*, 2022, **893**, 162334.
36 J. Mondal and S. K. Srivastava, *ACS Appl. Nano Mater.*, 2020, **3**, 11048–11059.
37 M. Z. A. Warshagha and M. Muneer, *ACS Omega*, 2022, **7**, 30171–30183.
38 J. Zou, K. Wu, H. Wu, J. Guo and L. Zhang, *J. Mater. Sci.*, 2020, **55**, 3329–3346.
39 S. Zeb, G. Sun, Y. Nie, H. Xu, Y. Cui and X. Jiang, *Mater. Adv.*, 2021, **2**, 6839–6884.
40 P. A. Shinde, A. C. Lokhande, N. R. Chodankar, A. M. Patil, J. H. Kim and C. D. Lokhande, *Electrochim. Acta*, 2017, **224**, 397–404.
41 M. S. Alshammari, W. H. Hassan, M. M. Al-Zahiwat, I. Mahariq, M. A. Ismail, Z. Atamuratova, S. Muminov and A. Amari, *J. Alloys Compd.*, 2025, **1021**, 179730.
42 S. Adhikari, D. Sarkar and G. Madras, *RSC Adv.*, 2015, **5**, 11895–11904.
43 X. Duan, S. Xiao, L. Wang, H. Huang, Y. Liu, Q. Li and T. Wang, *Nanoscale*, 2015, **7**, 2230–2234.
44 R. Venugopal, A. Dinakaran, M. C. Nair, A. C. Balachandran, N. D. Madhavan and B. Deb, *RSC Appl. Interfaces*, 2024, **1**, 1382–1394.
45 G. Lu, X. Li, P. Lu, H. Guo, Z. Wang, Q. Zhang, Y. Li, W. Sun, J. An and Z. Zhang, *Toxics*, 2024, **12**, 70.
46 F. Lei, Y. Sun, K. Liu, S. Gao, L. Liang, B. Pan and Y. Xie, *J. Am. Chem. Soc.*, 2014, **136**, 6826–6829.
47 C. Zhu, C. Li, M. Zheng and J.-J. Delaunay, *ACS Appl. Mater. Interfaces*, 2015, **7**, 22355–22363.
48 Y. Chen, Z. Huang, M. Zhou, Z. Ma, J. Chen and X. Tang, *Environ. Sci. Technol.*, 2017, **51**, 2304–2311.
49 P. Liu, J. Duan, Q. Ye, F. Mei, Z. Shu and H. Chen, *J. Catal.*, 2018, **367**, 115–125.
50 X. Li, J. Ma, L. Yang, G. He, C. Zhang, R. Zhang and H. He, *Environ. Sci. Technol.*, 2018, **52**, 12685–12696.
51 L. Yang, X. Zou, H. Wang, T. Chen, H. Liu, F. Sun and D. Chen, *Res. Chem. Intermed.*, 2025, **51**, 4559–4581.
52 S. Liu, H. Liu, G. Jin and H. Yuan, *RSC Adv.*, 2015, **5**, 45646–45653.
53 Q. Zhou, L. Zhang, P. Zuo, Y. Wang and Z. Yu, *RSC Adv.*, 2018, **8**, 36161–36166.
54 M. Ma, Y. Yang, Y. Chen, J. Jiang, Y. Ma, Z. Wang, W. Huang, S. Wang, M. Liu, D. Ma and X. Yan, *Sci. Rep.*, 2021, **11**, 2597.
55 P. A. Shinde, V. C. Lokhande, A. M. Patil, T. Ji and C. D. Lokhande, *Int. J. Hydrogen Energy*, 2018, **43**, 2869–2880.
56 Y. Baek and K. Yong, *J. Phys. Chem. C*, 2007, **111**, 1213–1218.
57 J. A. Pinedo-Escobar, J. Fan, E. Moctezuma, C. Gomez-Solís, C. J. Carrillo Martinez and E. Gracia-Espino, *ACS Omega*, 2021, **6**, 11840–11848.
58 J. Fu, Q. Xu, J. Low, C. Jiang and J. Yu, *Appl. Catal., B*, 2019, **243**, 556–565.
59 A. K. Nayak, R. Ghosh, S. Santra, P. K. Guha and D. Pradhan, *Nanoscale*, 2015, **7**, 12460–12473.
60 S. Bock, C. Kijatkin, D. Berben and M. Imlau, *Appl. Sci.*, 2019, **9**, 4933.
61 K. Sayama, H. Hayashi, T. Arai, M. Yanagida, T. Gunji and H. Sugihara, *Appl. Catal., B*, 2010, **94**, 150–157.
62 M. Zhou, X. Tian, H. Yu, Z. Wang, C. Ren, L. Zhou, Y.-W. Lin and L. Dou, *ACS Omega*, 2021, **6**, 26439–26453.
63 A. A. Tessema, C.-M. Wu and K. G. Motora, *ACS Omega*, 2022, **7**, 38475–38486.
64 C. Li, S. Yu, H. Dong, Y. Wang, H. Wu, X. Zhang, G. Chen and C. Liu, *J. Colloid Interface Sci.*, 2018, **531**, 331–342.
65 A. H. Nethercot, *Phys. Rev. Lett.*, 1974, **33**, 1088–1091.
66 R. S. Mulliken, *J. Chem. Phys.*, 1934, **2**, 782–793.
67 R. J. Zollweg, *J. Chem. Phys.*, 1969, **50**, 4251–4261.
68 E. Amouhadi, H. Aliyan, H. Aghaei, R. Fazaeli and D. Richeson, *Mater. Sci. Semicond. Process.*, 2022, **143**, 106560.
69 M. El-Kemary, H. El-Shamy and I. El-Mehasseb, *J. Lumin.*, 2010, **130**, 2327–2331.
70 M. Malakootian, A. Nasiri and M. Amiri Gharaghani, *Chem. Eng. Commun.*, 2020, **207**, 56–72.

71 N. H. Tran, M. Reinhard and K. Y.-H. Gin, *Water Res.*, 2018, **133**, 182–207.
72 Y. Nosaka and A. Y. Nosaka, *Chem. Rev.*, 2017, **117**, 11302–11336.
73 A. Nezamzadeh-Ejhieh and Z. Salimi, *Desalination*, 2011, **280**, 281–287.
74 F. Ghribi, M. Sehailia, L. Aoudjit, F. Touahra, D. Zioui, A. Boumechhour, D. Halliche, K. Bachari and Z. Benmaamar, *J. Photochem. Photobiol. Chem.*, 2020, **397**, 112510.
75 M. L. Tran, C. H. Nguyen, C.-C. Fu and R.-S. Juang, *J. Environ. Manage.*, 2019, **252**, 109611.
76 N. A. Mohd Razali, W. N. Wan Salleh, F. Aziz, L. W. Jye, N. Yusof and A. F. Ismail, *J. Clean. Prod.*, 2021, **309**, 127438.
77 A. Nasiri, F. Tamaddon, M. H. Mosslemin and M. Faraji, *MethodsX*, 2019, **6**, 1557–1563.
78 M. Farzadkia, E. Bazrafshan, A. Esrafili, J.-K. Yang and M. Shirzad-Siboni, *J. Environ. Health Sci. Eng.*, 2015, **13**, 35.
79 Y. Yang, B. Liu, J. Xu, Q. Wang, X. Wang, G. Lv and J. Zhou, *ACS Omega*, 2022, **7**, 6035–6045.
80 M. Zhou, X. Tian, H. Yu, Z. Wang, C. Ren, L. Zhou, Y.-W. Lin and L. Dou, *ACS Omega*, 2021, **6**, 26439–26453.
81 J. Zhang, X. Zan, X. Shen and H. Zheng, *Mater. Res. Bull.*, 2023, **165**, 112301.
82 S. Appu, Udayabhanu, B. R. Anusha, H. N. Priyadarshini, F. Alharethy, R. G. Srinivas, Abhijna, G. Nagaraju and K. Prashantha, *Mater. Chem. Phys.*, 2025, **337**, 130573.
83 Y. Nosaka and A. Nosaka, *ACS Energy Lett.*, 2016, **1**, 356–359.
84 D. Qin, C. Zhang, F. Qin, H. Weng, H. Luo, C. Huang, B. Wu and C. Chu, *Environ. Sci. Technol.*, 2026, **60**, 6276–6286.
85 K. Zhang, R. Wang, X. Zhong and F. Jiang, *ACS Omega*, 2024, **9**, 28422–28436.
86 W. N. Wan Ishak, H. L. Tan, N. F. Abu Bakar, N. Radacsi and Y. P. Lim, *RSC Adv.*, 2025, **15**, 24726–24738.
87 J. Yu, D. Sun, T. Wang and F. Li, *Chem. Eng. J.*, 2018, **334**, 225–236.
88 M. S. Islam, S. M. Hoque, M. Rahaman, M. R. Islam, A. Irfan and A. Sharif, *ACS Omega*, 2024, **9**, 10680–10693.
89 X. Kong, L. Cao, Y. Shi, Z. Chen, W. Shi and X. Du, *Molecules*, 2023, **28**, 5098.
90 S. Zulfiqar, S. Liu, N. Rahman, H. Tang, S. Shah, X. Yu and Q. Liu, *Rare Met.*, 2021, **40**, 2381–2391.
91 M. Zhou, X. Tian, H. Yu, Z. Wang, C. Ren, L. Zhou, Y.-W. Lin and L. Dou, *ACS Omega*, 2021, **6**, 26439–26453.
92 F. Ghribi, M. Sehailia, L. Aoudjit, F. Touahra, D. Zioui, A. Boumechhour, D. Halliche, K. Bachari and Z. Benmaamar, *J. Photochem. Photobiol. Chem.*, 2020, **397**, 112510.
93 G. O. El-Sayed, H. A. Dessouki, H. S. Jahin and S. S. Ibrahiem, *J. Basic Environ. Sci.*, 2014, **1**, 102–110.
94 M. Farzadkia, A. Esrafili, M. A. Baghapour, Y. D. Shahamat and N. Okhovat, *Desalination Water Treat.*, 2014, **52**, 4947–4952.
95 B. Farahani, M. Giahi, M. H. Ghorbani, R. Fazaeli and O. Moradi, *J. Nanostruct. Chem.*, 2023, **13**, 303–320.
96 N. Askari, M. Beheshti, D. Mowla and M. Farhadian, *Mater. Sci. Semicond. Process.*, 2021, **127**, 105723.